Results from prototype polarimeter/interferometer on Alcator C-Mod

By
Kelly Smith

Submitted to the Nuclear Science and Engineering Department in partial fulfillment for the degree of

Master of Science in Nuclear Science and Engineering

At the
MASSACHUSETTS INSTITUTE OF TECHNOLOGY
May 2007
[June 2007]

Author.....
Department of Nuclear Science and Engineering
May 18, 2007

Certified.....
James H. Irby
Principal Research Engineer
Alcator C-Mod Operations Group Leader
Thesis Supervisor

Certified.....
Ian H. Hutchinson
Chair, Department of Nuclear Science and Engineering
Thesis Supervisor

Accepted.....
Jeffrey Coderre
Chair, Committee on Graduate Students
Department of Nuclear Science and Engineering

Results from prototype polarimeter/interferometer on Alcator C-Mod

By
Kelly Smith

Submitted to the Nuclear Science and Engineering Department in partial fulfillment for the degree of

Master of Science in Nuclear Science and Engineering

Abstract

The poloidal field and corresponding toroidal current profiles have been among the most difficult and most important measurements in tokamak fusion research. One method demonstrated to obtain information about these quantities is polarimetry, in which Faraday rotation caused by the plasma is measured. Design has begun for a 20-channel, Far-infrared polarimeter-interferometer system on Alcator C-Mod. In preparation for this experiment, a poloidally-viewing prototype polarimeter-interferometer has been constructed, installed, and tested on Alcator C-Mod. This thesis describes the design of this prototype and reports the results obtained, with emphasis on those applicable to the future polarimeter-interferometer. Specifically, experimental techniques and alignment procedures, sensitivity to vibration, and conditions affecting reflection from the inner wall are explored.

Acknowledgements

I want to thank my advisor, Jim Irby. He has been extremely helpful and supportive throughout the years of work represented by this thesis. In addition, I would like to thank Rick Murray, Rick Leccacorvi, Rui Vieira and the entire C-Mod staff for their help.

Contents

List of Figures

List of Tables

Chapter I

Introduction

This thesis describes a prototype polarimeter experiment constructed and tested on the Alcator C-Mod tokamak. The work presented here is a predecessor to a full polarimeter-interferometer diagnostic that will provide measurements about the internal magnetic field and electric current in the plasma. In this chapter, motivation is presented for polarimetry measurements, starting from a description of the tokamak and its magnetic field and current. Next, a survey and discussion of polarimetry techniques and their pertinent constraints are provided. This is followed by a description of the Alcator C-Mod experiment. Finally, the prototype polarimeter is introduced.

At the outset, it is important to define the objectives of the prototype experiment reported in this thesis. This experiment was not expected to measure the internal magnetic field of tokamak plasmas. Rather, its purposes are to refine experimental techniques for measuring Faraday rotation and to assess experimental conditions that will be relevant to the future polarimeter-interferometer system. These conditions include the movement of the inner wall, survivability of in-vessel optics, and the sensitivity of results to optical alignment. This thesis describes the design and results of two polarimetry techniques and an interferometer configuration, as well as the performance of in-vessel optics.

1.1 Motivation

Since its inception in the late 1960's, the tokamak has emerged as the performance leader in magnetic confinement fusion. The largest tokamak experiments have demonstrated plasma energies above 15 kilo-electron volts (keV), and energy confinement times on the order of seconds. Tokamaks are planned for the next two generations of magnetic confinement fusion experiments, and hoped to demonstrate the viability of fusion as a potential energy source.

The tokamak consists of a torus-shaped plasma confined by a magnetic field, which is made up of a large toroidal component and a small poloidal component. A schematic of a tokamak is presented in Figure 1.1. In the figure and throughout the following discussion, the direction around the torus is designated toroidal, and the angular direction around the cross section is referred to as poloidal. Conventional magnetic field coils generate the primary toroidal field, which can be accurately measured by induction loops. This measurement is generally considered to be among the most reliable in the realm of tokamak diagnostics. In contrast, the poloidal field is induced by electric current driven around the plasma loop. While the total current passing through a given cross section can be accurately measured, the distribution of current and, equivalently, poloidal magnetic field, has proven to be one of the most difficult plasma parameters to diagnose. Accurate and reliable measurement of internal field and current profiles is important in the study of both macroscopic and microscopic instabilities, as well as in external current drive experiments.

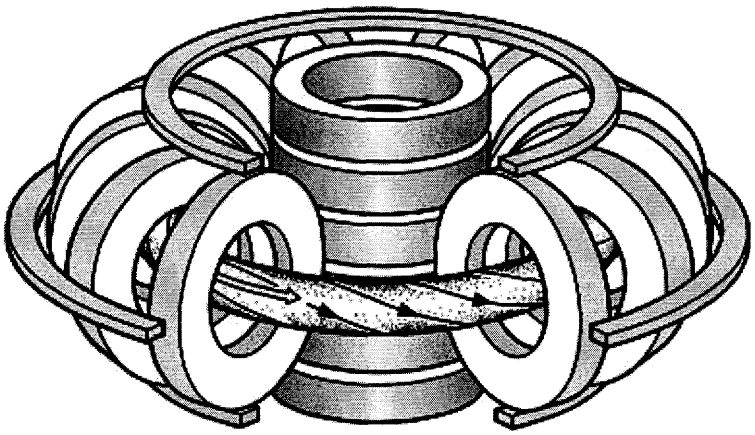

Figure 1.1 Schematic of tokamak coils, fields and plasma current [1]

While there is a wide array of applications in fusion plasma research that require knowledge of the poloidal magnetic field, two will be discussed here. First, the Kruskal-Shafranov limit derived from Magnetohydrodynamic (MHD) fluid theory imposes a constraint on poloidal field at the plasma core. The safety factor (q) is defined in a tokamak as the geometrically weighted ratio of poloidal and toroidal magnetic fields, expressed as: $q = \frac{rB_T}{RB_p}$, where r and R correspond to radial position in the poloidal and toroidal planes, respectively. The Kruskal-Shafronov limit states that in order for the plasma to be macroscopically stable, this quantity must remain greater than unity at all positions in the plasma.

Experimental observations have revealed the existence of sawtooth oscillations in the plasma core of many devices. These periodic fluctuations are measured as rapid drops in core density and temperature, followed by a gradual increase in these quantities

before the cycle repeats. Near the edge of the plasma, the oscillations are reversed; density and temperature are observed to gradually decrease between quick rises that are synchronized with the drops in the core (see Figure 1.2). The prevailing explanation for this phenomenon is that the current density on the plasma axis builds until the local safety factor reaches one, and a "crash" occurs—a local instability resulting from violation of the Kruskal-Shafronov limit. This instability quickly rearranges the plasma to satisfy the condition q>1 everywhere in the plasma. This explanation had not been tested directly due to the inability to accurately measure the poloidal field in the plasma core. However, recent measurements have suggested that a safety factor of less than one is possible, opening the topic for debate and necessitating reliable measurement of the core poloidal field.

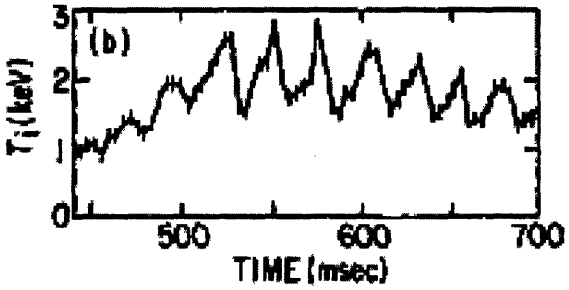

Figure 1.2 Sawtooth oscillations in core ion temperature trace [2]

Second, the envisioned fusion reactors of the future will operate in steady-state. At present, all operating tokamaks generate the poloidal field required for plasma confinement inductively. The essential concept is an electric transformer, with a core solenoid ramping up in voltage, and inducing a voltage and current in the plasma, which acts as the secondary loop. While this method has been reliable for generating tokamak plasmas, it is inherently pulsed and therefore undesirable from a power production

standpoint. In addition to a smooth energy output, steady state systems alleviate the engineering strain on materials associated with cyclic operation.

Achieving steady state tokamak operation will require some form of non-inductive current drive. One proposal for driving auxiliary current is the injection of a neutral beam that will impart its momentum through collisions with electrons, resulting in a net motion of electrons around the torus. A second technique is the damping of electromagnetic waves with specific phasing to impart energy to preferentially to electrons moving in one direction. Also, neoclassical transport theory describes the bootstrap current, a phenomenon resulting from the motion of particles trapped in "banana orbits" due to the curvature of tokamak field lines. The bootstrap current adds to the total toroidal current in a tokamak, and can be optimized under certain plasma conditions. Each of these active research areas aims to modify the current profile, and each can be benefited by accurate information about the distribution of plasma current.

1.2 Review of Polarimetry Techniques

The importance of experimental information about tokamak current profiles has led to many diagnostic efforts. For instance, the Motional Stark Effect (MSE) diagnostic has been demonstrated to provide localized measurements of magnetic field topology [3]. Equilibrium reconstructions have also been applied, in which measurements of edge magnetic fields are imposed on computational solutions of the equation for MHD equilibrium [4]. Another method that has been demonstrated to provide information about the field and current profile is polarimetry. As will be discussed in the next section, each of these techniques for obtaining poloidal field profiles has advantages and drawbacks, and each has a place in the diagnosis of tokamak plasmas. This thesis

describes a prototype polarimeter experiment, which makes use of the Faraday rotation of the polarization of an electromagnetic wave as it traverses the magnetized plasma. An introduction to this measurement technique is provided here.

De Marco and Segre proposed Faraday rotation as a means of measuring the poloidal magnetic field of a fusion plasma in 1972 [5]. The first polarimetry measurements on a tokamak were performed on TFR in 1978[6]. Around the same time, it was proposed to combine polarimetry and interferometry with a three-wavelength system [7][8]. Multi-chord polarimeter/interferometers in the far infrared (FIR) were shown to be operational on the TEXTOR tokamak in Germany [9] and the Joint European Torus (JET) [10]. Improvements in time resolution have allowed measurement of the q-profile during sawtooth oscillations. The safety factor was shown to stay below unity throughout the sawtooth period [11][12]. Polarimeter/interferometers have also been integrated into plasma control systems [13]. Time and spatial resolution have been improved on recent experiments. Results from the 11-chord FIR polarimeter/interferometer on the Madison Spherical Torus have provided detailed information about the peaking and broadening of the current profile during sawtooth crashes with a time resolution of 10 μs [14][15].

The experiments mentioned above have all been performed with source wavelengths in the far infrared (FIR) regime (50-200 μm). As will be discussed in Chapter 3, FIR is the appropriate choice of wavelength for modern tokamak applications where measurement of the poloidal field is the goal. Polarimetry has also been demonstrated as a means of determining plasma electron density by viewing along the well-known toroidal field. For this application in current large tokamaks, the optimal

wavelength choice is around 10 μm, readily available in off-the-shelf CO_2 lasers. Because this is the wavelength employed for the prototype polarimeter/interferometer described in this thesis, these experiments are explained in greater detail than those above.

Two methods for measuring Faraday rotation at 10.6 μm have been proposed as density diagnostics. Both methods were tested on the prototype polarimeter on Alcator C-Mod, and they will both be described in detail here. The first technique, suggested by Jobes and Mansfield [16], measures the phase difference between right- and left-handed circularly polarized beams propagating together through the plasma, analogous to the experimental method employed in some of the FIR experiments mentioned above. The optical layout of the Jobes design is found in Figure 1.3. Acousto-optic modulation is achieved with Bragg cells, resulting in three laser beams with slightly offset frequencies. One of these beams is reference and is propagated in air a distance equal to the plasma path, then combined with one of the plasma beams to form a heterodyne interferometer. The other two beams are given opposing circular polarizations, which acquire a relative phase difference during a double pass through the plasma. The Faraday rotation due to the plasma over the laser path is then obtained by measuring this phase difference between the two circular polarization components.

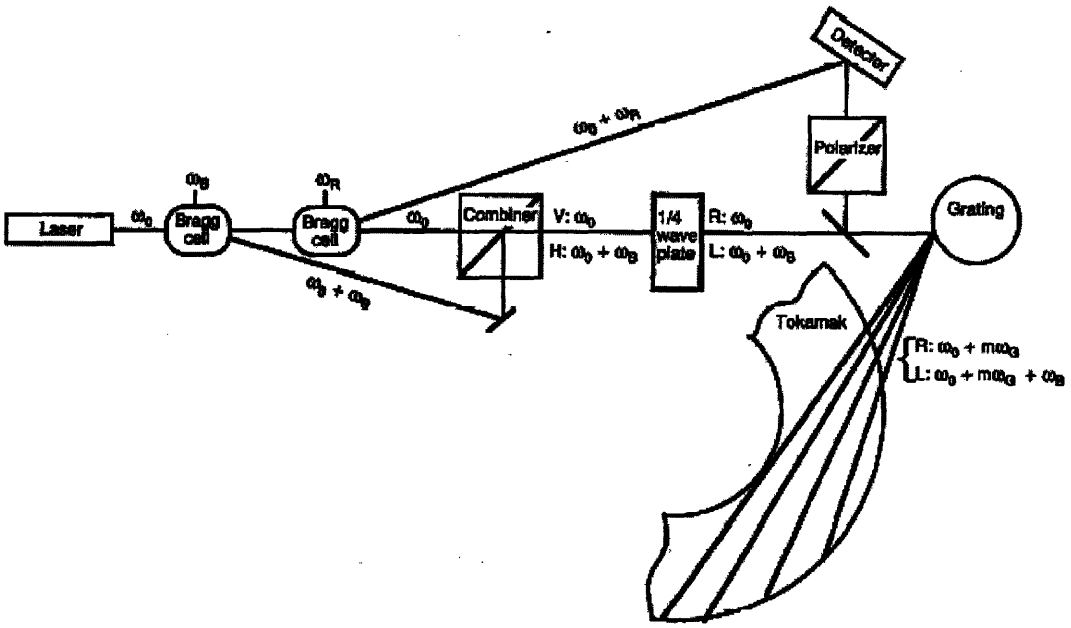

Figure 1.3 Layout of tangential polarimeter design proposed by Jobes [16]

The second technique, employed on the JT-60U Tokamak by Kawano [17], propagates a linearly polarized laser beam toroidally through the plasma and then measures the change in polarization angle caused by Faraday rotation. The polarimeter itself is based on the modulation of polarization by photo-elastic modulators. Figure 1.4 is a simplified schematic of the experimental setup for this technique. Although not depicted in the figure, two CO_2 lasers with different frequencies are used to provide vibration subtraction for interferometry. A heterodyne interferometer is also created in the same manner as in the Jobes design, again making use of acousto-optic frequency modulators. The Kawano scheme differs in the technique for measuring Faraday rotation; photoelastic polarization modulators combine with polarizers and IR detectors to make up a polarimeter identical to that used in current MSE experiments. Using this

method, the JT-60U group has obtained precision of a hundredth of a degree in rotation angle.

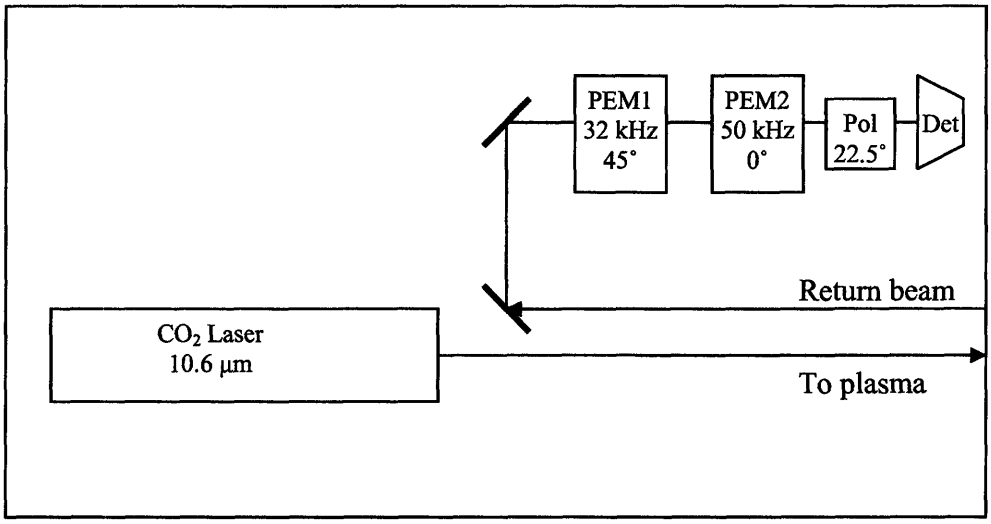

Figure 1.4 Simplified schematic of Kawano method for tangential polarimetry

1.3 Alcator C-Mod

Alcator C-Mod is a high-field, compact, divertor tokamak at MIT. It is unique because of its large toroidal magnetic field and capacity for confining high density plasmas, as well as its capacity among Ohmic devices for generating long plasma pulses relative to current relaxation times [18]. A summary of plasma parameters from the Alcator C-Mod design is found in Table 1.1 [19].

Toroidal Field (B_T)	9 Tesla
Electron Density (n_e)	10^{21} m^{-3}
Plasma Current (I_p)	3 MA
Minor Radius (a)	0.21 m

Major Radius (R_0)	0.67 m
Plasma Elongation (κ)	1.8
Triangularity (δ)	0.4

Table 1.1 Design parameters for Alcator C-Mod Tokamak [19]

As the plans for ITER have progressed beyond preliminary discussion and entered a phase of detailed design, there has been a growing interest among the fusion research community in Advanced Tokamak (AT) scenarios. This concept is essentially a modification of existing, Ohmically-driven tokamaks to longer plasma discharges that continue beyond inductive ramp-up. The central requirement for AT operation is non-inductive current drive. With this requirement in mind, research at Alcator C-Mod is moving toward controlled current profile scenarios [20]. As part of this research thrust, a lower hybrid current drive program has recently begun. Early results include a driven current approaching 1 MA, as well as evidence of sawtooth stabilization and central heating [21].

Poloidal field reconstructions for Alcator C-Mod are generated by the two-dimensional equilibrium code EFIT [4]. This fitting routine applies an iterative process to solve the Grad-Shafranov equation in two dimensions and match the solution with the experimentally determined boundary fields. While EFIT can generate a reconstruction of the poloidal magnetic field, its accuracy is significantly improved with additional information about internal plasma current [22].

A Motional Stark Effect (MSE) diagnostic has been installed and tested on Alcator C-Mod [23]. As mentioned above, this technique has been shown to provide

localized measurements of magnetic pitch angle; and hence provide poloidal field and current profiles [3]. However, the MSE system on Alcator C-Mod has faced numerous experimental difficulties [23]. Also, the technique depends on neutral beam penetration, which raises questions about its accessibility to information from the core of the large, high density machines of the future. Further, the difficulty of extracting profile information from raw data in both MSE and polarimetry experiments suggests the benefit of cross-correlating results between the two diagnostic techniques.

1.4 Prototype Polarimeter

A far-infrared, multichord polarimeter/interferometer is planned for installation on Alcator C-Mod in FY 2007. The most probable central wavelength is 119 μm, with two other wavelengths to allow for polarimetry and interferometry measurements to be made simultaneously. Approximately twenty beams will form a poloidal fan; they enter through a window on the outboard side of the tokamak and return along the same path after reflection from corner-cube retro-reflectors mounted on the inner wall (see Figure 1.5).

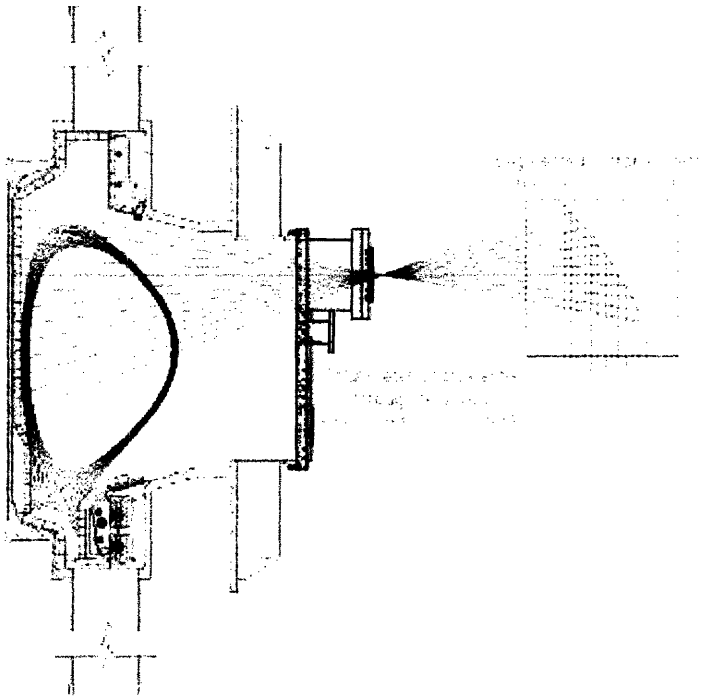

Figure 1.5 Schematic of poloidal plasma view accessible by 20-chord FIR polarimeter system

Several experimental constraints are important to investigate. For this purpose, a prototype polarimeter/interferometer was installed and tested on Alcator C-Mod. Operating at 10.6 μm, the prototype experiment is not ideal for measuring Faraday rotation under relevant plasma conditions [24]. However, the prototype includes many of the factors crucial to the FIR experiment and allows a study of these factors prior to the significant financial investment of a three-wavelength, 119 μm laser system.

First, the sensitivity of measurements to laser alignment was investigated for the two techniques discussed above. In addition, interferometry results have provided a quantitative description of vibration, particularly relating to the movement of the inner

wall. Finally, the survivability of optics on the inner wall of a tokamak has been analyzed.

The results reported in this thesis are also relevant to the plans for the poloidal-view, FIR polarimeter/interferometer that has been proposed for the International Thermonuclear Experimental Reactor (ITER) [25]. Polarimetry data will be an important tool for the study of internal instabilities and non-ohmic current drive, as well as many other plasma phenomena. Many of the experimental limitations explored by the prototype polarimeter and mentioned above will transfer to the planning of the FIR polarimeter on ITER.

Chapter II

Theory

Outlined below is the basic theory behind the prototype polarimeter/interferometer constructed on Alcator C-Mod. First, a simple model for wave propagation in a cold plasma is described and a dispersion relation is obtained. Faraday rotation is then derived using the plasma dispersion relation. In deriving this model, the Hutchinson textbook [22] and a review on polarimetry by Donne [26] were consulted; the reader is referred to these references for further discussion. Next, the theoretical foundation is given for the two polarimetry measurement techniques reported in this thesis. Finally, a brief discussion of interferometry is provided.

2.1 Plasma Model

The propagation of an electromagnetic wave in a plasma is governed by Maxwell's Equations coupled with a suitable plasma model. We will start with a general description of the fields, then choose the cold plasma approximation to obtain the plasma conductivity tensor, and finally arrive at a dispersion relation for the wave propagation.

The relevant equations for the electromagnetic wave propagation are Faraday's Law and Ampere's Law, coupled with Ohm's Law for an anisotropic medium. These are found in equations (2.1-3)

$$\nabla \times \vec{E} = -\frac{\partial \vec{B}}{\partial t} \qquad (2.1)$$

$$\nabla \times \vec{B} = \mu_0 \vec{J} + \frac{1}{c^2}\frac{\partial \vec{E}}{\partial t} \tag{2.2}$$

$$\vec{J} = \vec{\sigma} \cdot \vec{E} \tag{2.3}$$

Combining these three equations gives a non-linear relationship for the wave electric field, in which all the information about the medium is contained in the conductivity tensor $\vec{\sigma}$.

$$\nabla \times \nabla \times \vec{E} + \frac{\partial}{\partial t}\left[\mu_0 \vec{\sigma} \cdot \vec{E} + \frac{1}{c^2}\frac{\partial \vec{E}}{\partial t}\right] = 0 \tag{2.4}$$

We will now assume plane-wave solutions for the fields, represented as: $\vec{E} = \vec{E}_0 e^{i(\vec{k}\cdot\vec{r}-\omega t)}$. Under this assumption, $\nabla \longrightarrow i\vec{k}$ and $\frac{\partial}{\partial t} \longrightarrow i\omega$, and we obtain:

$$\left[\vec{k}\vec{k} - k^2\vec{I} + \frac{\omega^2}{c^2}\left(\vec{I} + \frac{i}{\omega\varepsilon_o}\vec{\sigma}\right)\right] \cdot \vec{E} = 0 \tag{2.5}$$

Defining the dielectric tensor, $\vec{\varepsilon} \equiv \vec{I} + \frac{i}{\omega\varepsilon_o}\vec{\sigma}$ we can now write down and expression for the dispersion relation.

$$\det\left[\vec{k}\vec{k} - k^2\vec{I} + \frac{\omega^2}{c^2}\vec{\varepsilon}\right] = 0 \tag{2.6}$$

To proceed, we will need to apply a model for the plasma and obtain the dielectric tensor defined above. Because the frequencies employed for polarimetry are much higher than the plasma frequency, we will neglect both the motion of plasma ions and thermal forces. This is the cold plasma approximation. We will then assign a Cartesian coordinate system such that the wave vector for the incident radiation aligns with the z-direction, and the magnetic field is assumed to lie in the y-z plane.

We begin with the electron momentum equation, which we linearize by assuming the same plane wave expansion as for the fields:

$$n_e m_e \frac{d\vec{v}}{dt} = -n_e e\left[\vec{E} + \vec{v} \times \vec{B}\right] \tag{2.7}$$

$$i\omega m_e \vec{v} = e\left[\vec{E} + \vec{v} \times \vec{B}\right]$$

Imposing the geometry described above and solving for the three components of velocity, we obtain:

$$v_x = \frac{e}{i\omega m_e}\frac{1}{1-Y^2}\left[E_x - (iY\cos\theta)E_y + (iY\sin\theta)E_z\right]$$

$$v_y = \frac{e}{i\omega m_e}\frac{1}{1-Y^2}\left[(iY\cos\theta)E_x + (1-Y^2\sin^2\theta)E_y - (Y^2\sin\theta\cos\theta)E_z\right]$$

$$v_z = \frac{e}{i\omega m_e}\frac{1}{1-Y^2}\left[-(iY\sin\theta)E_x - (Y^2\sin\theta\cos\theta)E_y + (1-Y^2\cos^2\theta)E_z\right]$$

Here we have defined the angle between the incident wave vector and the magnetic field as θ and represented the ratio of the electron cyclotron frequency to the laser frequency as Y, where the usual formula for cyclotron frequency has been utilized.

In order to obtain a dielectric tensor to insert in the dispersion relation (Eq. 2.6), we need a relationship between particle velocity and plasma conductivity, which is found in the plasma current. Again neglecting ion motion, and returning to the Ohm's Law expression (Eq. 2.3) used in the previous section, we have:

$$\vec{J} = -en_e\vec{v} = \vec{\sigma}\cdot\vec{E}$$

The plasma conductivity and dielectric tensors can then be obtained from the velocity solution above:

$$\vec{\sigma} = \frac{-n_e e^2}{i\omega m_e}\frac{1}{1-Y^2}\begin{bmatrix} 1 & -iY\cos\theta & iY\sin\theta \\ iY\cos\theta & 1-Y^2\sin^2\theta & Y^2\sin\theta\cos\theta \\ -iY\sin\theta & Y^2\sin\theta\cos\theta & 1-Y^2\cos^2\theta \end{bmatrix}$$

$$\vec{\varepsilon} \equiv \vec{I} + \frac{i}{\omega\varepsilon_o}\vec{\sigma} = \vec{I} - \frac{X}{1-Y^2}\begin{bmatrix} 1 & -iY\cos\theta & iY\sin\theta \\ iY\cos\theta & 1-Y^2\sin^2\theta & Y^2\sin\theta\cos\theta \\ -iY\sin\theta & Y^2\sin\theta\cos\theta & 1-Y^2\cos^2\theta \end{bmatrix}, \qquad \textbf{(2.8)}$$

$$X = \frac{\omega_{pe}^{\ 2}}{\omega^2} = \frac{n_e e^2}{m_e \varepsilon_0 \omega^2}$$

$$Y = \frac{\omega_{ce}}{\omega} = \frac{eB}{m_e \omega}$$

With a full dispersion relation expressed in terms of plasma parameters, we are now able to calculate the polarizations of the electromagnetic waves that propagate in the plasma. To do this, we insert the dielectric tensor (Eq. 2.8) into Eq. 2.5:

$$\left\{ \vec{n}\vec{n} - n^2\vec{I} + \vec{I} - \frac{X}{1-Y^2}\begin{bmatrix} 1 & -iY\cos\theta & iY\sin\theta \\ iY\cos\theta & 1-Y^2\sin^2\theta & Y^2\sin\theta\cos\theta \\ -iY\sin\theta & Y^2\sin\theta\cos\theta & 1-Y^2\cos^2\theta \end{bmatrix} \right\} \cdot \begin{pmatrix} E_x \\ E_y \\ E_z \end{pmatrix} = 0$$

Here we have defined the refractive index, $\vec{n} = \frac{\vec{k}c}{\omega}$. Remembering that we have chosen our coordinate system so that the wave vector has only a z-component, dividing by E_y and introducing the variables $\alpha = \frac{E_x}{E_y}$ and $\beta = \frac{E_z}{E_y}$, we can write down the matrix equation we need to solve to determine the characteristic polarizations.

$$\begin{bmatrix} 1-n^2-\frac{X}{1-Y^2} & \frac{iXY\cos\theta}{1-Y^2} & -\frac{iXY\sin\theta}{1-Y^2} \\ -\frac{iXY\cos\theta}{1-Y^2} & 1-n^2-\frac{X(1-Y^2\sin^2\theta)}{1-Y^2} & -\frac{XY^2\sin\theta\cos\theta}{1-Y^2} \\ \frac{iXY\sin\theta}{1-Y^2} & -\frac{XY^2\sin\theta\cos\theta}{1-Y^2} & 1-\frac{X(1-Y^2\cos^2\theta)}{1-Y^2} \end{bmatrix} \cdot \begin{pmatrix} \alpha \\ 1 \\ \beta \end{pmatrix} = 0$$

Solving this system of equations gives a quadratic equation for α that can be solved using the quadratic formula.

$$\alpha^2 + \frac{iY\sin^2\theta}{(1-X)\cos\theta}\alpha + 1 = 0$$

$$\alpha = -\frac{iY\sin^2\theta}{2(1-X)\cos\theta} \pm i\sqrt{\frac{Y^2\sin^4\theta}{4(1-X)^2\cos^2\theta} + 1} = \frac{E_x}{E_y}$$

Assuming the laser frequency is much higher than the plasma frequency implies that the quantity 1-X is approximately unity. Under this assumption, $\frac{E_x}{E_y} = \pm i$ when the condition $\frac{Y}{\cos\theta} << 1$ is satisfied. Thus, under this condition, the characteristic waves have circular polarization about the direction of beam propagation. For 119 μm and a magnetic field of 5T, $Y = \frac{\omega_{ce}}{\omega} = 0.06$. Consequently, the characteristic polarizations are circular for all angles except those very close to perpendicular to the magnetic field.

To calculate the index of refraction for each of the circular polarizations, we begin with a general expression for the cold plasma dispersion relation, known as the Appleton-Hartree formula:

$$N_\pm^2 = 1 - \frac{X(1-X)}{1 - X - \frac{1}{2}Y^2\sin^2\theta \pm \left[\left(\frac{1}{2}Y^2\sin^2\theta\right)^2 + (1-X)^2Y^2\cos^2\theta\right]^{1/2}} \quad \textbf{(2.8)}$$

Taking X and Y to be small, this reduces to:

$$\begin{aligned} N_\pm^2 &\approx 1 - \frac{X}{1 \pm Y\cos\theta} \approx 1 - X(1 \mp Y\cos\theta) \\ N_\pm &\approx \sqrt{1-X}\left[1 \pm \frac{XY\cos\theta}{1-X}\right]^{1/2} \\ N_\pm &\approx \sqrt{1-X}\left[1 \pm \frac{XY\cos\theta}{2(1-X)}\right] \end{aligned} \quad \textbf{(2.9)}$$

2.2 Faraday Rotation

When a material has a different refractive index for right- and left-handed circular polarizations, it is said to be optically active. Optical activity caused by a magnetic field parallel to the axis of propagation through the material is Faraday rotation. This effect describes the change in polarization angle of linearly polarized light as it propagates through the medium. We will first describe Faraday rotation in a uniform magnetized material, and then expand the treatment to include a tokamak plasma.

Assigning a Cartesian coordinate system where the direction of the laser beam propagation is $\hat{z}$ and the polarization vector aligns with $\hat{x}$, we can first express the linearly polarized wave in circularly polarized components:

$$\vec{E}(0) = E_0\hat{x} = \frac{\vec{E}_+ + \vec{E}_-}{2}$$
$$\vec{E}_\pm \equiv E_0(\hat{x} \mp i\hat{y})$$

These components are now propagated a distance z through the medium with their respective wave numbers.

$$\vec{E}(z) = \frac{1}{2}\left[\vec{E}_+ e^{ik_+ z} + \vec{E}_- e^{ik_- z}\right]$$
$$\vec{E}(z) = \frac{1}{2} e^{\frac{i(k_+ + k_-)z}{2}}\left[\vec{E}_+ e^{\frac{i(k_+ - k_-)z}{2}} + \vec{E}_- e^{\frac{-i(k_+ - k_-)z}{2}}\right]$$

Returning to Cartesian coordinates, we find that the polarization is still linear, but has rotated an angle α from the initial state:

$$\vec{E}(z) = E_0 e^{\frac{i(k_+ + k_-)z}{2}}\left[\frac{\hat{x}}{2}\left(e^{\frac{i(k_+ - k_-)z}{2}} + e^{\frac{-i(k_+ - k_-)z}{2}}\right) + \frac{\hat{y}}{2i}\left(e^{\frac{i(k_+ - k_-)z}{2}} - e^{\frac{-i(k_+ - k_-)z}{2}}\right)\right]$$

$$\vec{E}(z) = E_0 e^{\frac{i(k_+ + k_-)z}{2}}\left(\hat{x}\cos\alpha + \hat{y}\sin\alpha\right)$$

$$\alpha = \frac{(k_+ - k_-)z}{2} = \frac{\omega}{2c}(N_+ - N_-)z$$

Thus we obtain the Faraday rotation effect for an arbitrary, optically active medium. This result can be applied to the cold plasma discussed in Section 2.1 by substituting the approximate refractive indices for left- and right-handed circular polarizations (Eq. 2.9). Expressing all quantities in terms of plasma parameters, we obtain:

$$\alpha = \frac{\omega}{2c}\left(\sqrt{1-X}\left[1 + \frac{XY\cos\theta}{2(1-X)}\right] - \sqrt{1-X}\left[1 - \frac{XY\cos\theta}{2(1-X)}\right]\right)z$$

$$\alpha = \frac{\omega}{2c}\frac{XY\cos\theta}{\sqrt{1-X}}z \approx \frac{\omega}{2c}\frac{\omega_{pe}^2}{\omega^2}\frac{\omega_{ce}}{\omega}z\cos\theta$$

In the last step, we have again assumed X<<1. We can now insert the definitions of plasma and cyclotron frequencies to obtain:

$$\alpha = \frac{1}{8}\frac{e^3}{\pi^2 \varepsilon_0 m_e^{\,2} c^3}\lambda^2 n_e B z \cos\theta \qquad \textbf{(2.10)}$$

If we assume a wavelength much shorter than the scale length of plasma variations, we can apply the WKBJ approximation and insert values for physical constants to arrive at the well known expression for Faraday rotation in a plasma:

$$\alpha = 2.62\times10^{-13}\lambda^2 \int n_e \vec{B}\cdot d\vec{l} \qquad \textbf{(2.11)}$$

2.3 Measurement of Faraday Rotation

Two different techniques have been applied to measure Faraday rotation in the work described in this thesis. Both have been used on other experiments, the choice of method depending on experimental factors such as expected rotation and available optical components for the chosen wavelength. The theory behind each of these methods is described below, following the treatments of Veron [8], Dodel and Kunz [27], and Kemp [28]. The practical application of these two techniques is discussed in Chapter 3.

2.3.1 Dodel Kunz technique

Faraday rotation depends on the optically active nature of a magnetized plasma; counter-rotating circularly polarized beams acquire a relative phase difference as they propagate. Dodel and Kunz have demonstrated a measurement technique in which two laser beams with an offset in frequency are given opposing circular polarizations. These two beams then follow the same path through the plasma and are analyzed and measured, where the phase shift between them corresponds to the Faraday rotation.

We first consider two laser beams with equal amplitudes, a small frequency offset and opposing circular polarizations:

$$\vec{E}_1 = \frac{E}{2}[\cos(\omega t)\hat{x} + \sin(\omega t)\hat{y}]$$

$$\vec{E}_2 = \frac{E}{2}[\cos((\omega + \Delta\omega)t)\hat{x} - \sin((\omega + \Delta\omega)t)\hat{y}]$$

$$\omega >> \Delta\omega$$

A superposition of these beams gives a single beam with its plane of polarization rotating at a frequency $\frac{\Delta\omega}{2}$.

$$\vec{E}_1 + \vec{E}_2 = \frac{E}{2}\{[\cos(\omega t) + \cos((\omega + \Delta\omega)t)]\hat{x} + [\sin(\omega t) - \sin((\omega + \Delta\omega)t)]\hat{y}\}$$

$$\vec{E}_1 + \vec{E}_2 = E\cos\left((\omega + \frac{\Delta\omega}{2})t\right)\left[\cos\left(\frac{\Delta\omega}{2}t\right)\hat{x} - \sin\left(\frac{\Delta\omega}{2}t\right)\hat{y}\right]$$

Measuring the intensity of either linear polarization component of this beam gives the usual beat pattern for two waves with shifted frequencies:

$$P \propto E^2 \cos(\Delta\omega t)$$

As this superposition travels through the plasma, $\vec{E}_1$ and $\vec{E}_2$ acquire different phases corresponding to their different refractive indices.

$$\vec{E}_1(z) + \vec{E}_2(z) = E\cos\left((\omega + \frac{\Delta\omega}{2})t - \frac{(k_+ + k_-)z}{2}\right)\left[\cos\left(\frac{\Delta\omega}{2}t + \frac{(k_+ - k_-)z}{2}\right)\hat{x} - \sin\left(\frac{\Delta\omega}{2}t + \frac{(k_+ - k_-)z}{2}\right)\hat{y}\right]$$

$$\vec{E}_1(z) + \vec{E}_2(z) \approx E\cos(\omega t - \vartheta)\left[\cos\left(\frac{\Delta\omega}{2}t + \alpha\right)\hat{x} - \sin\left(\frac{\Delta\omega}{2}t + \alpha\right)\hat{y}\right]$$

Here we have made use of the assumption that the frequency shift is much smaller than the central laser frequency and labeled the global phase shift acquired in the plasma as φ and the Faraday rotation angle α. The intensity of either the x- or y-component of this beam therefore depends on Faraday rotation angle α, which can be deduced by comparing the phase of either linear polarization component before and after passing through the plasma.

2.3.2 Photo-elastic modulation technique

An alternate method for measuring Faraday rotation is a direct measure of polarization angle. Specifically, this measurement has been shown to achieve excellent resolution through modulation of the polarization of linearly polarized light.

We first send a linearly polarized laser beam through the plasma, where it acquires a rotation in polarization plane. If the x-direction is assigned to the polarization of the incident light, then the wave coming out of the plasma after rotating an angle α can be expressed as:

$$\vec{E} = E_0[\cos\alpha\hat{x} + \sin\alpha\hat{y}]$$

The light then traverses a photo-elastic modulator (PEM), which imposes a sinusoidal oscillation in polarization angle. If the PEM modulation amplitude is A_0 and frequency is Ω, then the resulting wave field is:

$$\vec{E} = E_0\left[\cos\alpha e^{iA/2}\hat{x} + \sin\alpha e^{-iA/2}\hat{y}\right]$$
$$A = A_0\cos\Omega t$$

A polarizer oriented at 45° with respect to the x-axis then allows a measurement of the original polarization angle.

$$\vec{E}_{\text{det}} = \left\{\frac{1}{\sqrt{2}}(\hat{x}+\hat{y})\cdot E_0\left[\cos\alpha e^{iA/2}\hat{x} + \sin\alpha e^{-iA/2}\hat{y}\right]\right\}\frac{1}{\sqrt{2}}(\hat{x}+\hat{y})$$
$$\vec{E}_{\text{det}} = \frac{E_0}{2}\left[\cos\alpha e^{iA/2} + \sin\alpha e^{-iA/2}\right](\hat{x}+\hat{y})$$
$$P_{\text{det}} = |E|^2 = \frac{E_0}{2}(1+\sin 2\alpha\cos A)$$

This expression for the power at the detector can be expanded in Bessel function coefficients:

$$P_{\text{det}} = \frac{E_0}{2}[1+\sin 2\alpha\cos(A_0\cos\Omega t)]$$
$$P_{\text{det}} \approx \frac{E_0}{2}[1 + J_0(A_0)(\sin 2\alpha) + 2J_2(A_0)\cos 2\Omega t(\sin 2\alpha)] \qquad \textbf{(2.12)}$$

By choosing a modulation amplitude that is a zero of the lowest order Bessel function, and measuring both the static signal and the second harmonic of the modulation

frequency, we can extract the polarization angle. The zero of the Bessel function is 0.383 waves (2.405 radians), which eliminates the second term of Equation 2.12. The signal from the detector can then be written as a DC term and a term that oscillates at the second harmonic of the PEM modulation, whose amplitude is referred to here as "V_{2f}." In Volts, this signal can be expressed as:

$$V_{\text{det}} = V_{DC} + V_{2f}\cos 2\Omega t = \frac{E_0}{2}\left[1 + 2J_2(A_0)\cos 2\Omega t(\sin 2\alpha)\right]$$

Independent measurements of each of these signals allow the Faraday rotation to be deduced. In the calculation below, the Faraday rotation angle is assumed to be small and a factor of $\sqrt{2}$ has been inserted to account for the RMS value read by the lock-in amplifier.

$$\begin{aligned} \frac{V_{2f}}{V_{DC}} &= 2J_2(2.405)\sin 2\alpha \approx 4J_2(2.405)\alpha \\ \alpha &= 93.8\frac{V_{2f}}{V_{DC}} \end{aligned} \qquad \textbf{(2.13)}$$

2.4 Interferometry

The theory of interferometry as a measurement technique for electron density in tokamak plasmas has been discussed thoroughly by Veron [8]. An application of this treatment to the TCI experiment on Alcator C-Mod is found in the doctoral dissertation of Thomas Luke [29]. Because the interferometer configuration of the prototype experiment is modeled after the TCI diagnostic, the underlying theory is the same. The introduction below is sufficient to understand and interpret the results presented in this thesis; however, the reader is referred to the references mentioned for a more detailed treatment.

Analogous to the description above, we first consider an electromagnetic wave propagating in a plasma. With either a poloidal or a vertical view, the direction of propagation is roughly normal to the toroidal magnetic field. In the specific case of the prototype interferometer, the laser polarization is parallel to the magnetic field, allowing us to immediately apply the solution to the cold plasma dispersion relation known as the "ordinary wave." The derivation is not presented here, but can be found in numerous textbooks, including Stix [30]. For the ordinary wave, the index of refraction is:

$$N = \sqrt{1 - \omega_{pe}^2 / \omega^2}$$

As the plane wave passes through the plasma, it acquires a phase shift that depends on the plasma frequency, and thus, the electron density. This phase is then measured by comparison with a reference beam that propagates through air a distance equal to that traversed by the plasma-probing beam. If the distance traveled is represented by Δz, the phase difference between the plasma and reference beams is:

$$\varphi = \left(N_{reference} - N_{plasma}\right)\frac{\omega \Delta z}{c} = \left[1 - \left(1 - \omega_{pe}^2 / \omega^2\right)^{1/2}\right]\frac{\omega \Delta z}{c}$$

$$\varphi \approx \frac{\omega_{pe}^2}{2c\omega}\Delta z$$

Here we have inserted the value of refractive index in air as unity, and assumed that the laser frequency is much higher than the plasma frequency. We can now express this phase difference as a line integral in terms of plasma parameters, and then insert numerical values for physical constants to arrive at the widely used expression for interferometry measurements.

$$\varphi = \frac{e^2 \lambda}{4\pi m_e c^2 \varepsilon_0} n_e(z)\Delta z \rightarrow 2.82 \times 10^{-15} \lambda \int n_e(z) dz \qquad \textbf{(2.14)}$$

To make this measurement, a heterodyne scheme is typically applied, in which the plasma and reference beams have different frequencies. Consider the following expressions for the electric fields of the plasma beam at the original frequency, and the reference beam with a frequency offset $\Delta\omega$, where $\omega >> \Delta\omega$. We will assume equal power in each arm of the interferometer for simplicity.

$$E_{plasma} = \frac{E}{2}\cos(\omega t - \vartheta)$$

$$E_{reference} = \frac{E}{2}(\cos(\omega + \Delta\omega)t)$$

The power detected is then proportional to the square of the sum of these fields, which can be expanded and simplified by looking only at the terms oscillating slowly compared to the fundamental laser frequency.

$$P \propto \frac{E^2}{4}\left\{\cos^2(\omega t - \vartheta) + \cos^2(\omega + \Delta\omega)t + 2\cos(\omega t - \vartheta)\cos(\omega + \Delta\omega)t\right\}$$

$$P \propto \frac{E^2}{4}\left\{\cos^2(\omega t - \vartheta) + \cos^2(\omega + \Delta\omega)t + 2\cos((2\omega + \Delta\omega)t - \vartheta) + \cos(\Delta\omega t + \vartheta)\right\}$$

$$P_{slow} \propto \frac{E^2}{4}[1 + \cos(\Delta\omega t + \vartheta)]$$

In the final step, the third term averages to zero and the first two terms average to one-half when viewed over many periods. The remaining term can now be compared with the beat frequency between the reference beam and a local oscillator at the fundamental laser frequency ω to obtain the phase difference φ found in Equation 2.14.

Chapter III

Experimental Design

This chapter describes the prototype polarimeter as it was designed and implemented on Alcator C-Mod. Two general configurations were tested. First, a polarimeter and interferometer were constructed with a poloidal view, using corner-cube retro-reflectors to return the laser beams for detection. The designs for these experiments are discussed in parts, beginning with the components on the laser table and then moving to the components that allow access to the plasma. Finally, polarimetry measurements were made on the Two-color Interferometer (TCI) experiment already in operation on Alcator C-Mod. A brief introduction to TCI concludes this chapter.

3.1 Table components

The radiation source is a natural starting point for the discussion of a polarimetry experiment. Several attributes of wave propagation in plasmas, as well as experimental conditions of a tokamak, impose limitations on the choice of radiation source. The availability of lasers in the desired wavelength range also constrains the selection.

Recalling that the Faraday rotation angle depends on the square of the wavelength, we can establish a range of wavelengths that will produce large enough signal to be measured (usually tens of degrees) but not so much rotation that a periodic ambiguity arises (less than 180°). Depending on plasma parameters and viewing geometries, this range typically corresponds to the mid to far infrared.

Second, the effects of refraction must be considered. For waves with frequencies much higher than the plasma frequency, propagation through the plasma approaches the

free space limit. At laser frequencies approaching the plasma frequency, the plasma acts as a refractive medium. Because plasma frequency (proportional to electron density) is constant in neither space nor time during a plasma discharge, the result is an effective change in alignment that compromises results. This effect is more pronounced at longer wavelengths.

An additional factor is the vibration of optical components. Because of the size and complexity of modern fusion experiments, a polarimeter design must take into account the inevitable acoustic and mechanical noise present in the system. With path lengths on the order of tens of meters, small angular motion of optical surfaces can significantly disrupt laser alignment and limit experimental accuracy. Alignment problems caused by vibrations become less severe as wavelength is increased.

As documented in the Master's Thesis of Erik Tejero [25], the appropriate choice of wavelength for a poloidally-viewing polarimeter on Alcator C-Mod is the far infrared (>50 μm). Using this wavelength, Faraday rotation angles are predicted to be on the order of ten degrees in magnitude. Further, this wavelength is long enough that the effect of vibrations on alignment will allow adequate experimental precision, with noise levels of a few hundredths of a degree. Refraction is a concern for source wavelengths in the far infrared, but should still be acceptable for a practical experiment. Table 3.1 is a list of calculated values of misalignment due to refraction for paths through the plasma corresponding to the chords illustrated in Figure 3.1. This calculation was performed through ray-tracing–numerically calculating the angular deviation of a ray for a series of small steps along the path. By inserting a density profile that exceeds characteristic parameters of an Alcator C-Mod plasma (parabolic shape with peak density 5×10^{20} m^{-3}),

the refractive index for each point in the plasma is known, allowing a geometrical treatment of refraction of the laser beam. The values listed below correspond to a wavelength of 119 μm. For each ray, the table lists the calculated position in the major radius and vertical directions for the beam's reflection at the inner wall; as well as the vertical position corresponding to the non-refractive case (straight path). The final column lists the difference in vertical position caused by refraction.

Ray	R(mm)	Z(mm)	Zinter(mm)	delZ(mm)
1	449.8	400.2	400.0	0.2
2	450.0	376.6	376.1	0.5
3	450.0	353.2	352.3	0.9
4	449.9	329.4	328.6	0.8
5	449.8	305.8	305.1	0.7
6	449.8	282.3	281.6	0.7
7	450.0	258.8	258.2	0.7
8	449.8	235.4	234.8	0.6
9	449.9	212.0	211.4	0.6
10	449.7	188.6	188.1	0.6
11	449.7	165.2	164.7	0.5
12	449.7	141.8	141.3	0.5
13	450.0	118.5	117.8	0.8
14	449.8	95.0	94.2	0.7
15	450.0	71.3	70.6	0.8
16	449.8	47.4	46.8	0.7
17	449.9	23.4	22.8	0.6
18	449.7	−0.9	−1.2	0.4
19	449.8	−25.3	−25.5	0.2
20	449.9	−50.0	−50.0	0.0

Table 3.1 Calculated displacements due to refraction for chords in Figure 3.1 [31]

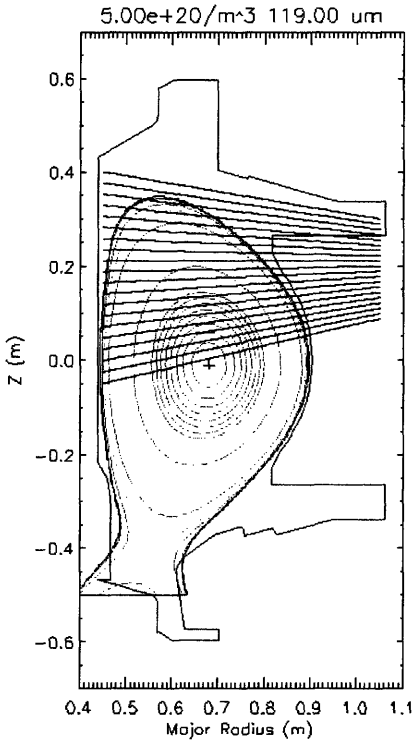

Figure 3.1 Plasma cross section used for refraction calculations. Chords are numbered from top to bottom [31]

As mentioned in Chapter 1, the radiation source for the prototype polarimeter/interferometer described in this thesis is a CO_2 laser, with wavelength 10.6 μm. This selection was made based on the availability of lasers and optical components,

as well as the capacity for studying the experimental factors that will pertain to the FIR polarimeter to be constructed on C-Mod. Refraction, for instance, is negligible at 10.6 μm, allowing a careful study of inner wall movement with a certainty that the vacuum alignment corresponds to the alignment with plasma present. Although the Faraday rotation angle at this wavelength is too small to measure with the resolution available, it was possible to compare measurement techniques and identify sensitivity to optical alignment. These results are discussed in Chapter 4.

3.1.1 Lasers

Two CO_2 lasers were employed in the experiments described below. Initially, a Synrad industrial laser was used. This laser generates a continuous wave, 20 Watt beam at 10.6 μm. Near the end of the run campaign in which this laser was employed, a mode instability was discovered, in which the frequency of the emitted beam fluctuates on a time scale of a few Hertz. This effect was most apparent after passage through an Acousto-optic modulator, in which the angular deviation of a frequency offset beam depends on the input frequency. After several weeks of laser operation, the modulated beam could be seen to move up to a centimeter when viewed over a path length of a few meters. This instability contributed to slow changes in alignment that caused signal drifts several times larger than the signal itself.

To remedy this problem, a laser was obtained from Coherent and employed in the prototype polarimeter. With a base power of 60 W, this laser is expected to provide a better signal-to-noise ratio, which is of particular importance as in-vessel optics lose reflectivity throughout the run campaign. Because this laser is designed for scientific rather than industrial applications, its mode stability meets specified expectations for this

experiment. This laser has been tested independently, but has not been used for the results presented in this thesis. However, it is identical to the source laser for TCI, and therefore makes up part of the experimental design described in the last section of this chapter.

3.1.2 Detectors

The detectors employed for measurements at the CO_2 wavelength are photovoltaic cells that operate at room temperature. This choice eliminates the need for an independent cooling system, which can introduce additional noise to the experiment. However, the threshold signal size measurable with these detectors is not as low as for cooled detectors, leading to the eventual replacement with thermo-electrically cooled photovolatics.

For the experiments reported below, the detectors employed were produced by VIGO. These detectors were specifically designed to operate at 10.6 μm. Bench testing confirmed that they meet the specified sensitivity of 1.2 Amps/Watt, and have a response time capable of tracking 100 kHz oscillations.

3.1.3 Optical Layouts

This section describes the three optical configurations employed with a poloidal view: interferometer, polarimeter with counter-rotating beams, and polarimeter with modulated measurement. For each layout, a schematic of the optical paths is provided, along with a description of key components. In addition, the pertinent electronics are explained.

The basic principle of interferometry is the measurement of a relative phase shift between a reference and a plasma beam. A schematic of the interferometer employed in this work can be found in Figure 3.2. The source of the primary electromagnetic wave is the Synrad CO_2 laser described above. A second frequency is generated with an acousto-optic modulator (AOM), which drives a sound wave in a refractive medium that acts like a rotating diffraction grating. The output is a beam at the fundamental laser frequency and approximately half the input power, and a diffracted beam of the same power with an angular offset and a frequency equal to the laser frequency plus the modulator drive frequency. In this experiment, the offset is 40 MHz.

In addition to the CO_2 wavelength, a Helium-Neon (HeNe) laser is present for vibration subtraction. This laser provides a beam in the visible (633 nm). This beam is also passed through an acousto-optic modulator to result in four separate beams, each with a unique frequency. These four beams are then aligned such that the two zero order beams and the two first order beams propagate together. The mechanism for combining these wavelengths is a Zinc-Selenide beam combiner, which reflects almost perfectly at 633 nm and transmits almost perfectly at 10.6 μm.

Because of the sensitivity of interferometry measurements to this alignment, it is appropriate to discuss it here in greater detail. As illustrated below in the machine components section, the plasma-probing beam will traverse several meters as it travels from the optical table to the in-vessel reflectors, and back. The CO_2 and HeNe beams must be coaligned over the entire path in order to obtain an accurate measurement. This requirement imposes a narrow range of allowable angular error. In order to meet this alignment criterion, several conditions must be met. First, the two beams exiting each of

the AOM's must be made to propagate parallel to each other over a distance of 4-5 meters. Second, the pair of beams exiting each of the two the AOM's must be equally spaced. Because the visible wavelength is significantly less refractive than the infrared, the HeNe beams must be propagated much further than the CO_2 beams to obtain the same spacing. In this experiment, the beam centers were spaced 0.75 inches apart, which required approximately two passes (12 feet) across the optical table by the HeNe beams. The two sets of parallel beams are obtained by altering the alignment of each beam independently with small mirrors.

The final two conditions are that the CO_2 and HeNe beams be aligned perpendicularly and that they coincide on the surface of the beam combiner optic. These two conditions can be tested together by viewing the output close to the beam combiner and several meters away. This alignment can be achieved by iterating between the translational position of the beam combiner and its angle of incidence.

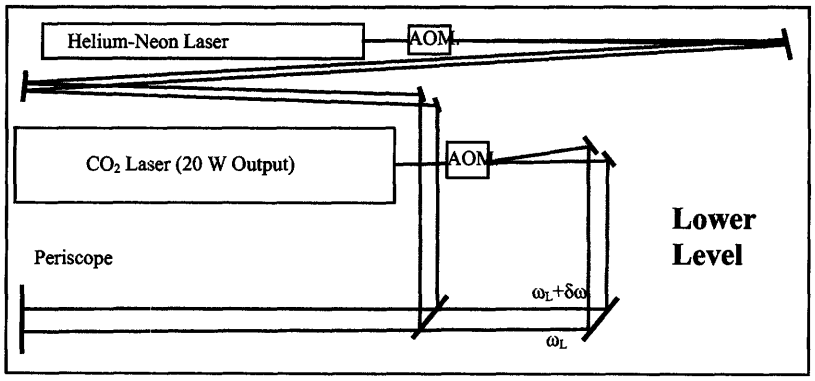

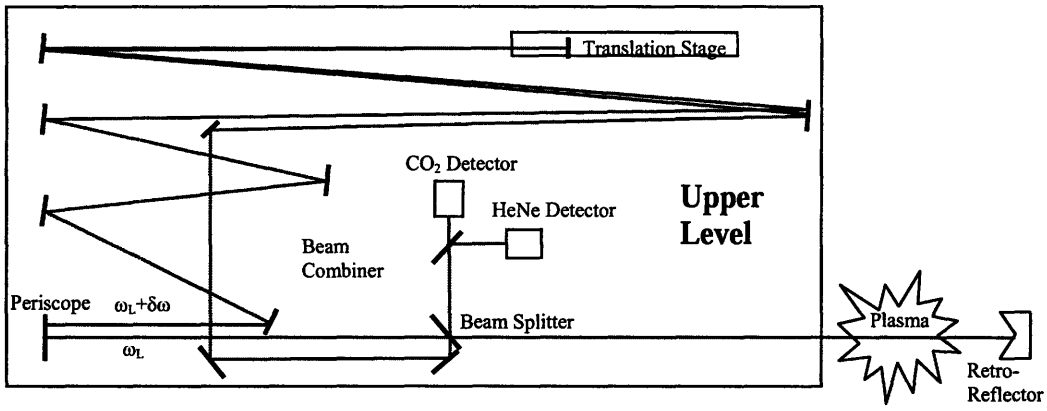

Figure 3.2 Optical layout of prototype interferometer. Beams propagate from lower level to upper level via a periscope illustrated in the lower left of each layout.

The two parallel beams, each consisting of a CO_2 and HeNe component, are now propagated through a periscope to the upper level of the optical table. Here a typical heterodyne interferometer is employed, with the frequency shifted beam acting as a reference and the fundamental propagating through the plasma and returning via corner-cube retro-reflectors mounted on the tokamak inner wall. The beams are combined with a 50-50 beam splitter, and the CO_2 and HeNe components are separated with a second beam combiner.

The vacuum signal on each detector is sinusoidal at the frequency of the acousto-optic modulator, 40 MHz. As illustrated in Figure 3.3 below, these signals are amplified and beat against the AOM drive signals. Phase demodulators count and digitize the resulting beat fringes. The fringe output is normalized to be zero in the vacuum case and to correspond to the line integral of electron density when the plasma is present.

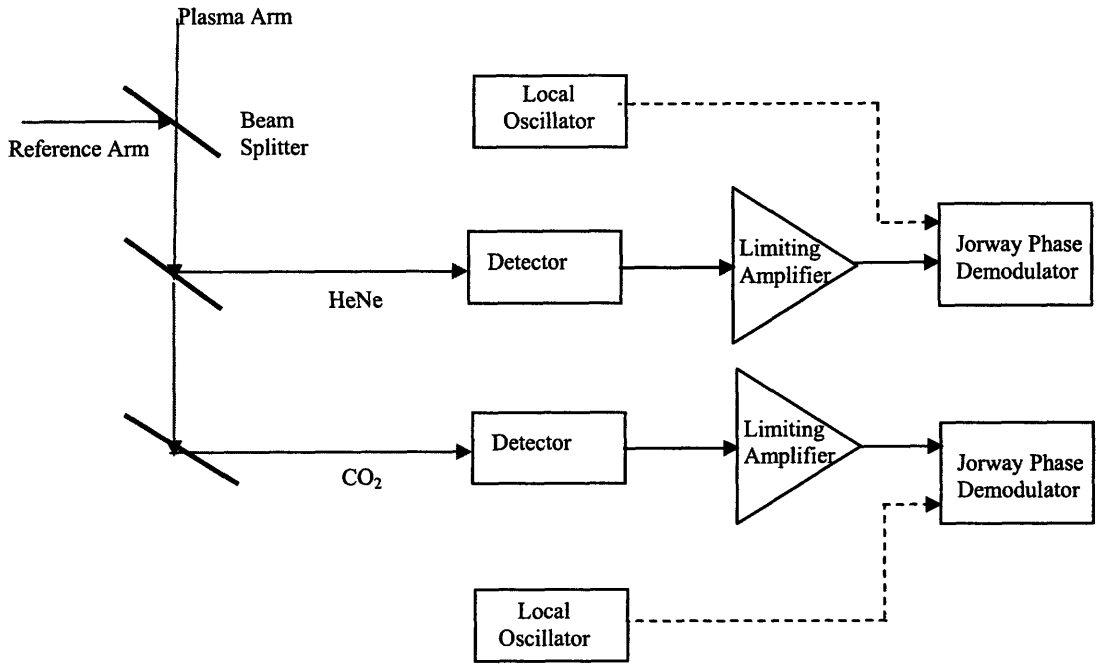

Figure 3.3 Schematic of electronics for prototype interferometer

As mentioned above, the purpose for the second wavelength is to enable vibration subtraction. All optical systems include an inherent noise level, or motion of the optical surfaces. As these surfaces move in the direction of beam propagation, they effectively alter the system path length and therefore affect the measured phase. Compensation for this effect is achieved by introducing a second wavelength, measuring the total phase shift (plasma and vibrational) with each wavelength, then calculating the phase shift caused by the plasma. For a detailed description of vibration subtraction using two colors, see the PhD dissertation of Thomas Luke [31].

Counter-rotating Technique

The first polarimetry technique tested is based on a straightforward application of some of the FIR systems described in Chapter 1. At 10.6 μm, the two frequencies

required for this measurement can be generated by a CO_2 laser and the acousto-optic modulator described above in the discussion of the interferometer configuration. However, instead of separating the two beams into a reference and plasma arm, as in the interferometer case, here the polarized beams are modified to create one beam with rotating polarization. Figure 3.4 is a schematic of the optical layout employed in this measurement.

The initial polarization of the laser output is parallel to the plane of the table, which will be denoted "X" in the following discussion. To generate the desired counter-rotating beam, the modulated frequency beam is picked off and passed through a half-wave plate, which rotates the polarization by 90°. This beam is now polarized in the direction perpendicular to the plane of the table, denoted "Y." These two beams are now combined with a thin-film polarizer, a zinc-selenide crystal oriented at Brewster's angle with respect to the incident beam. Because the crystal transmits the Y-polarization and reflects the X-polarization, the result is a coalignment of the two beams at their respective frequencies and polarizations. Transmission through a quarter-wave plate then changes the two linear polarizations to counter-rotating circular polarizations, which can now be expressed (see Chapter 2) as a single beam with the polarization vector rotating at half the modulation frequency, or 20 MHz.

The components represented within the dashed square in the figure make up the most sensitive part of this configuration. If, for example, one of the pickoff mirrors were to move independently of another, a misalignment would result between the two counter-rotating beams. Since the path lengths to the machine are on the order of a few meters, even a small misalignment can significantly compromise results. For this reason, these

optical components are connected by a single steel block that supports the individual mounts. In addition, the path between optics in this region is deliberately minimized. Similarly, the small pick-off mirrors for the modulated and unmodulated beams are a potential source of misalignment, and are therefore supported by single blocks and placed close together.

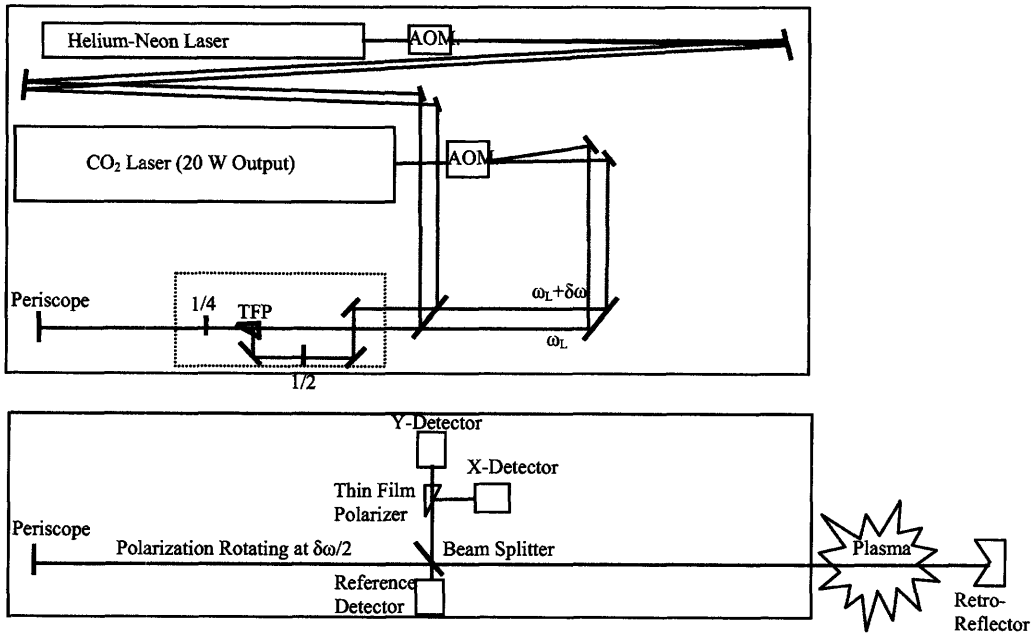

Figure 3.4 Optical layout of counter-rotating polarimeter configuration

This beam is propagated to the upper level, where a beam splitter sends half the power to a reference detector and the remaining half through the train of optics leading to the plasma, where Faraday rotation occurs. The purpose of this reference detector is to monitor amplitude variations corresponding to experimental uncertainties. Because it is located before the beam exits the optical table, the measurement here is a means of diagnosing the source of noise in the overall system, dividing between vibrations and electronic noise on the optical table and mechanical vibrations in the beam line and inner

wall retro-reflectors. Finally, the beam is returned to the optical table using retro-reflectors and analyzed after separating the return beam into X and Y polarization components. Although measurement of either polarization is sufficient, both components are detected to allow for mutual verification.

As in the interferometry measurement, the signals from the detectors are amplified and mixed with a local oscillator with a frequency of 40 MHz. Phase demodulators are again employed to digitize the fringe count caused by Faraday rotation in the plasma. Figure 3.5 is a diagram of the signal processing involved in this measurement.

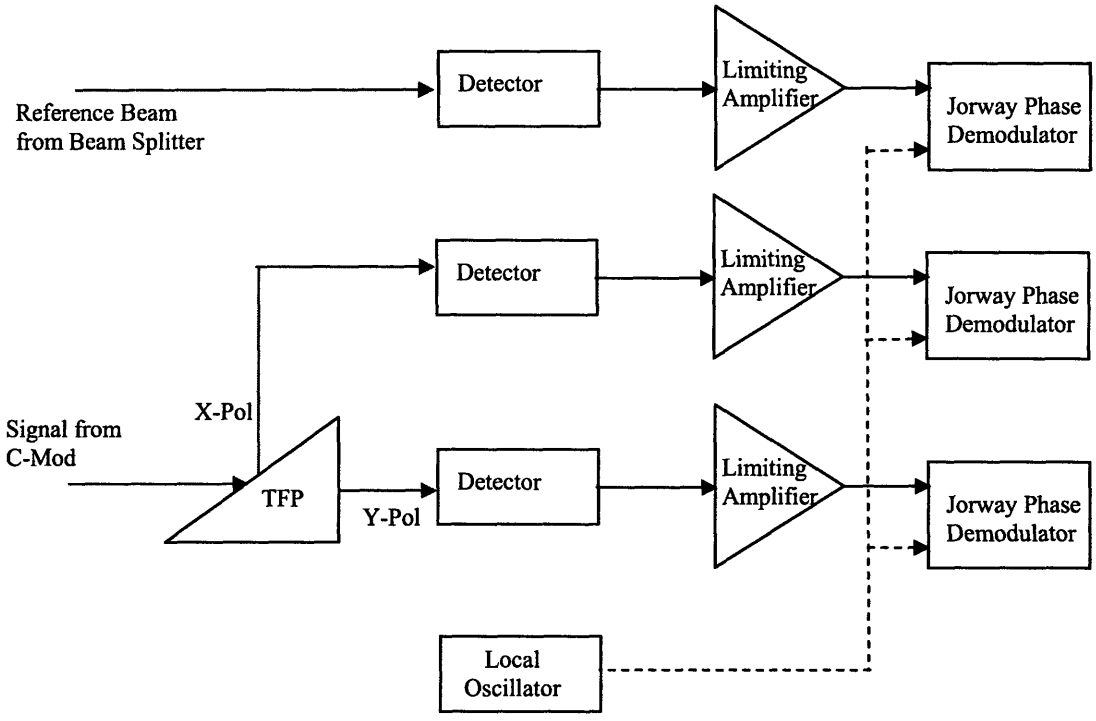

Figure 3.5 Schematic of electronics for counter-rotating beam polarimeter configuration

PEM technique

An alternate technique used to measure Faraday rotation closely follows the method used by the Kawano group on JT-60U. In this approach, a single laser beam with

linear polarization passes through the plasma and acquires a small rotation in polarization vector. This rotation is measured by modulation of the return beam polarization according to the theory outlined in Chapter 2. The schematic for this technique is found in Figure 3.6.

Like the other two configurations presented above, the light source is the Synrad 20 W CO_2 laser. In this technique, however, acousto-optic modulation is not required and the beam is simply inserted into the plasma, where it again reflects from in-vessel optics and returns to a beam splitter. The return beam is modulated using a photo-elastic modulator (PEM) driven sinusoidally at 50 kHz. This device, depicted in photograph below, introduces a periodic modulation in polarization as the laser light passes through a crystal whose birefringence varies with the oscillating electro-mechanical stress. While the PEM employed in this experiment is capable of half-wave modulation (i.e. alternating between linear polarization states), for this measurement a modulation amplitude of 0.383 waves was selected. This choice simplifies the calculation of Faraday rotation angle, as discussed in Chapter 2.

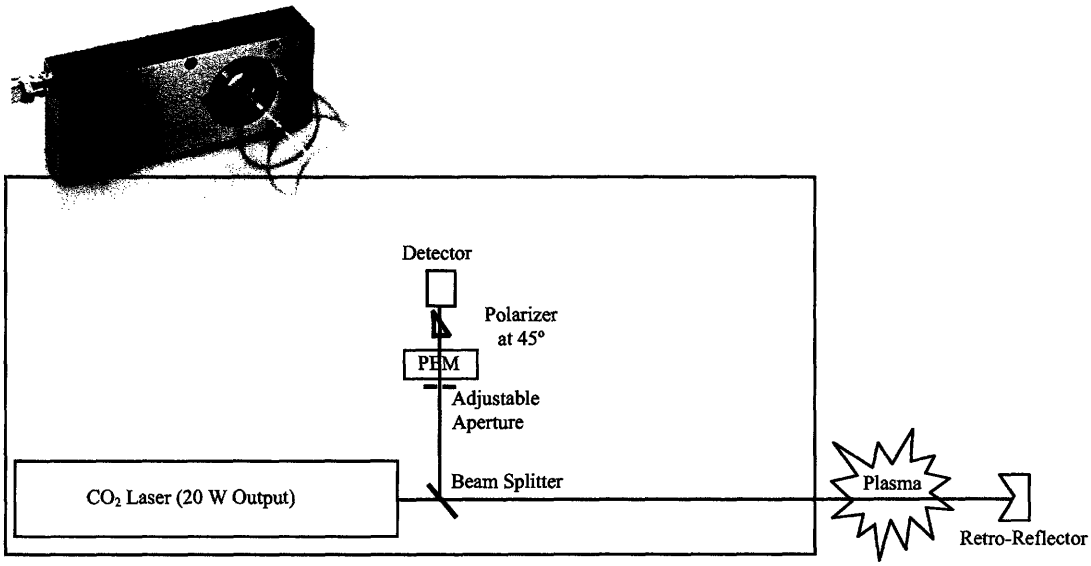

Photo courtesy of hindsinstruments.com

Figure 3.6 Optical layout of PEM polarimeter configuration

After modulation, the light passes through a polarizer oriented at 45° with respect to the plane of the table, and is detected with the same semiconductor detectors described above. As explained in Chapter 2, Faraday rotation is proportional to the ratio of the signal component at twice the modulation frequency to the DC signal component. These components can be obtained in two ways, both represented in Figure 3.7. First, the raw signal is sent to both a lock-in amplifier (using the 50 kHz modulation signal as a reference), and an amplifier-filter combination. Utilizing the option to lock in to the second harmonic, the lock-in amplifier gives the signal component at twice the PEM frequency, and the filtered output of the amplifier gives the DC component. These two signals are digitized using a 12 bit digitizer sampling at 10 kHz, then digitally divided and scaled to provide Faraday rotation angle.

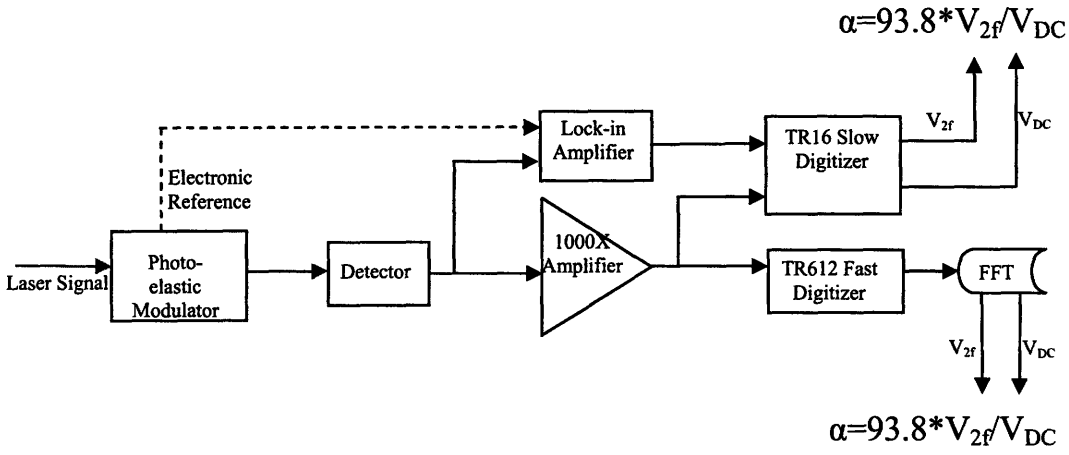

Figure 3.7 Schematic of electronics for PEM polarimeter configuration

Alternatively, the raw signal output from the detector can be amplified and digitized directly, then processed by Fast Fourier Transform (FFT) to obtain the DC and 2f components. This method requires significantly more memory and faster digitization capabilities than the lock-in amplifier technique. However, it is less sensitive to the inherent timescales and bandwidth limitations of the lock-in amplifier itself. Because of limited digitizer memory, the first method was primarily employed for the PEM results described below.

3.2 Machine Components

After careful alignment of the laser beams on the optical table, the primary objective in designing the remainder of the system is stability against the random vibrations present in the tokamak experiment. To this end, the optical path from the table to the window involves the fewest distinct components possible, each mounted to the concrete igloo surrounding Alcator C-Mod to provide maximum stability. A diagram of this path is found in Figure 3.8.

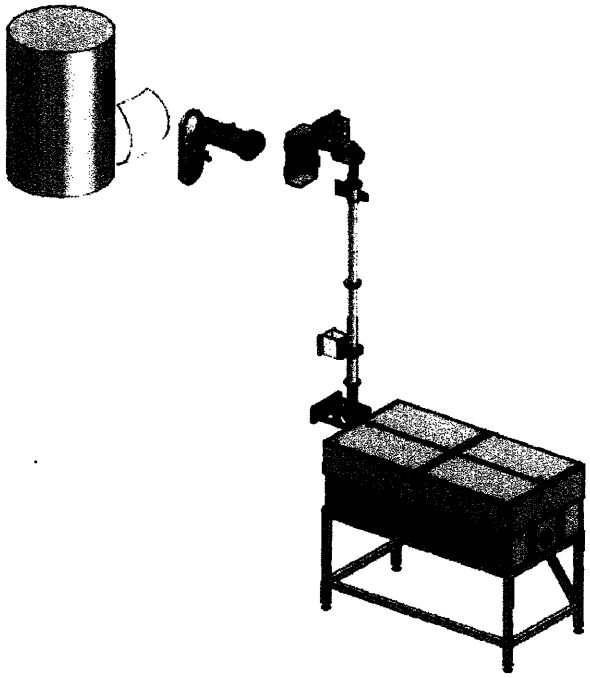

Figure 3.8 Prototype polarimeter system

The path is essentially comprised of a series of 90° reflections, each mounted solidly to the free-standing, concrete "igloo" surrounding the Alcator C-Mod vacuum vessel. By mounting to the igloo, the optics are not coupled to the various mechanical oscillations of the machine itself. Black-anodized aluminum pipe encloses the entire path to confine stray beams for safety purposes, as well as to eliminate the effects of random air currents and acoustic disturbances in the beam line. At the top of the pipe, a series of folding mirrors directs the beam to a final mirror, which is situated on a track that allows vertical motion to provide access to each of the six retro-reflectors on the inner wall of the tokamak. This track and final mirror are accessible through a hinged cover to a black-anodized aluminum box, which is also mounted to the concrete igloo. Figure 3.9 is a more detailed drawing of this track and mirror. It is important that this mirror allow both vertical and horizontal motion in order to direct the beam to the appropriate reflector

and compensate for slight changes in alignment in the system below. The horizontal range also allows for a deliberate toroidal component to the line of sight through the plasma, which could be used to examine Faraday rotation due to the large toroidal field, and null this effect in order to view only poloidally. While this configuration was briefly tested, the inadequate resolution and drifts in signal prohibited the observation of toroidal effects. All the results reported below were obtained using a view along the tokamak major radius.

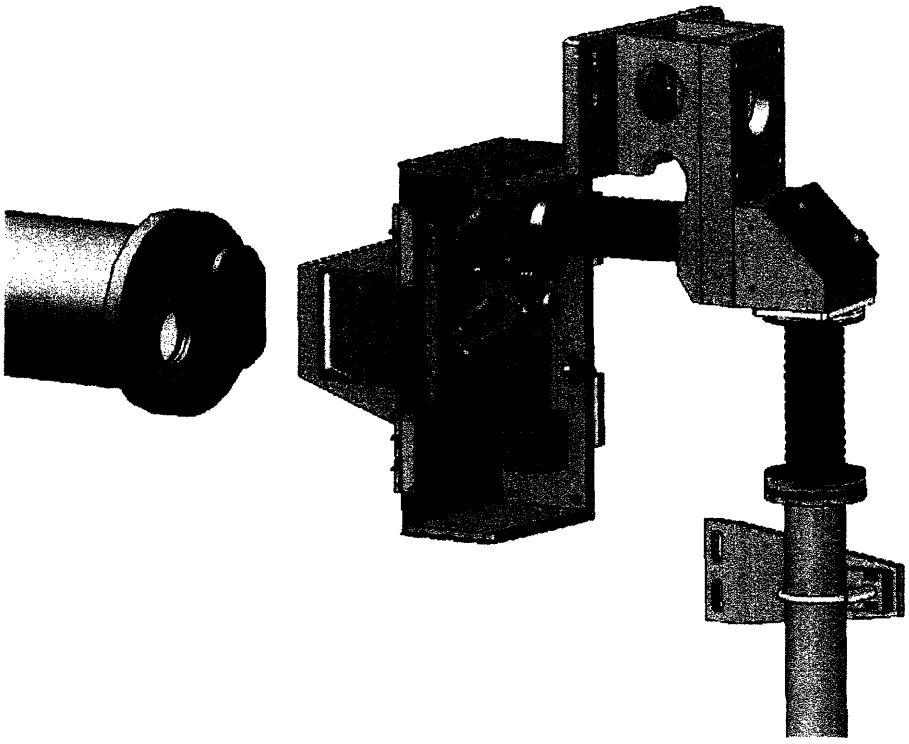

Figure 3.9 Close-up view of polarimeter beamline at vacuum vessel window

Translational motion along the track, combined with the capability to rotate the mirror in the vertical plane, allow the experimenter to choose from the six corner-cube

retro-reflectors mounted in a vertical array along the inner wall of Alcator C-Mod. Figure 3.10 demonstrates this range, illustrating only the two ends.

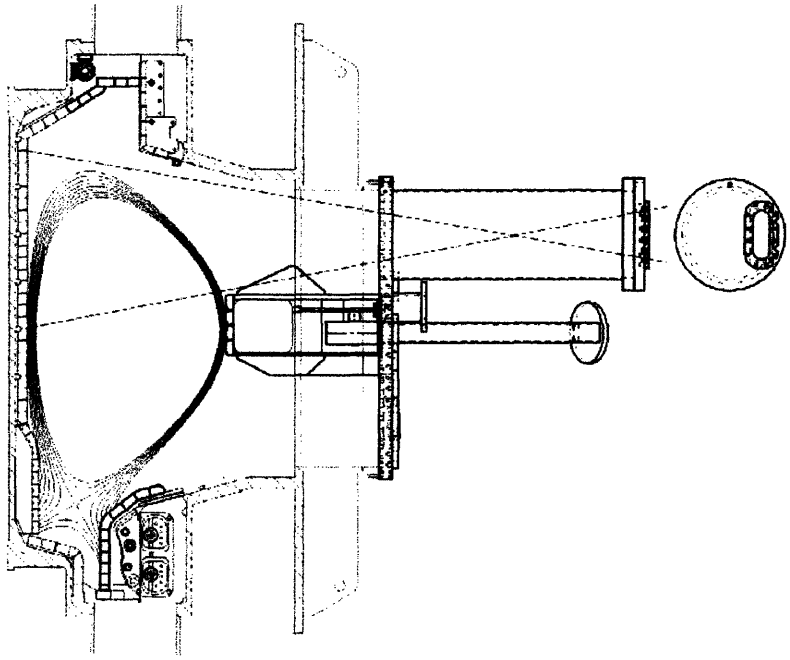

Figure 3.10 Range of possible polarimeter viewing chords. Only the two extremes are depicted, with four more possible chords distributed in between

A photograph of the retro-reflector array is found in Figure 3.11. Each reflector is mounted in the place of one molybdenum tile, with a bolting assembly attached to the inner wall structure. Vertical locations were chosen such that the viewing chords would evenly span the upper half of the plasma cross section, with the lowest retro-reflector just above the midplane for a typical discharge and the highest reflector just out of the plasma. Figure 3.12 displays the locations and mounting of the retro-reflector array. The measurements are in inches from the magnetic axis.

Figure 3.11 Photograph of retro-reflectors on the inner wall of Alcator C-Mod

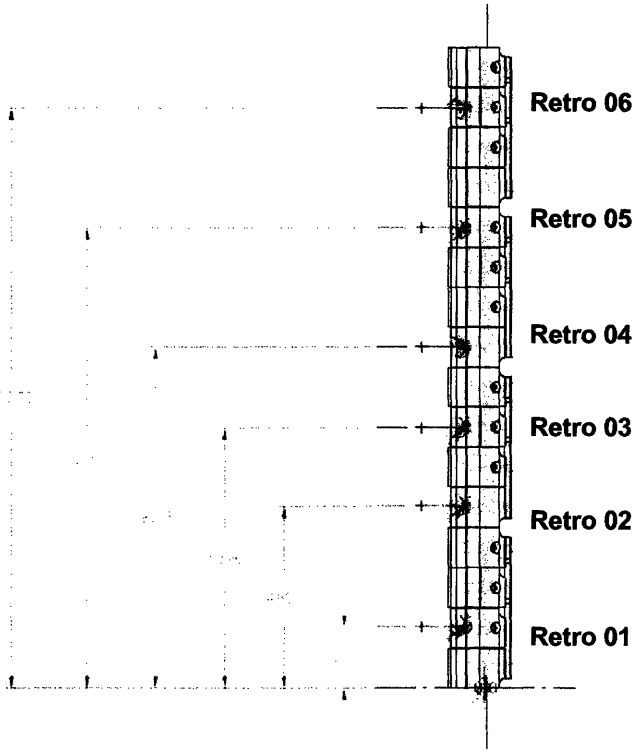

Figure 3.12 Diagram of retro-reflector positions (in inches)

For the experiments reported in this thesis, the retro-reflectors employed are hollow corner-cube retro-reflectors that are available through a commercial vendor. The optics are constructed from BK7 glass and coated with gold, which has a 98% reflectivity at 10.6 μm and slightly less at 633 nm. Each reflector is composed of three identical parts that form right angles with each other at the central junction, analogous to the inside of a cube. The specified perpendicularity of these surfaces is less than 10 arc seconds; and testing confirmed that each retro-reflector returns a symmetric beam after propagation over a path length comparable to the actual experiment. The reflectors are cylindrical in shape, with an open aperture of a half-inch diameter. Figure 3.13 is a

photograph of an unused retro-reflector, and Figure 3.14 is a composite drawing of the assembly.

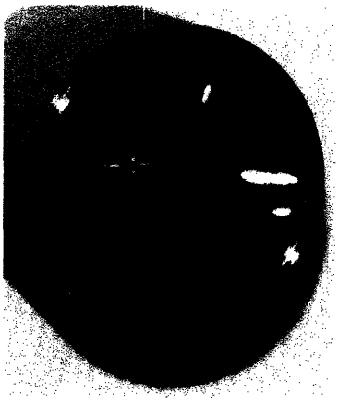

Figure 3.13 Photograph of an unused retro-reflector

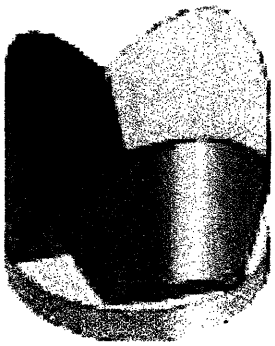

Figure 3.14 Drawing of retro-reflector assembly

Assessing the survivability of these optics on the inner wall is an important objective of this work. While retro-reflectors have been used in tokamak research, they have not been demonstrated to tolerate the harsh conditions of the inner wall. The most restrictive engineering constraints are addressed generally here, followed by a more specific discussion based on experimental results in Chapter 4.

First, thermal effects are a concern. The tokamak inner wall contains magnetic field coils that must be cooled for successful operation. In the case of Alcator C-Mod, the coils are copper and liquid nitrogen cooling maintains adequately low resistivity throughout the plasma discharge. Next-generation machines like ITER use superconducting coils, which require liquid helium temperatures for cooling. Further, the plasma itself contains large amounts of stored energy which can be deposited locally and non-uniformly across the first material surface. In Alcator C-Mod, plasmas typically contain up to 250 kilojoules; and the designs for ITER reach several Megajoules. These

two effects combine to present harsh extremes in operating temperature, leading to significant changes in the dimensions of assembly parts due to thermal expansion and contraction. The result could be a loss of alignment, or even the breaking of fragile parts like glass.

A second effect to consider is the coating of optical surfaces by dust and other macroscopic objects in the plasma. Several conditions can lead to a loss of plasma stability and a disruption, in which large electric currents run through the materials comprising the plasma container (walls, tiles, antennas, etc.). When disruptions occur, large amounts of dust are deposited around the vessel. In addition, tokamak surfaces are routinely coated with low-Z materials to improve plasma performance. In Alcator C-Mod, boron is locally deposited along the inner wall and other areas. Both ambient dust and the injections of boron can form a coating on optical surfaces and thereby deteriorate reflectivity.

Finally, sputtering by plasma-generated neutrals can destroy optical surfaces. While a majority of plasma components are ionized, there is always a small population of neutral atoms present. In the case of Alcator C-Mod, where plasmas normally consist of a Deuterium majority and a Hydrogen minority, these neutrals can be Deuterium or Hydrogen atoms, as well as impurity atoms like Carbon, Oxygen, or Molybdenum. Since there is a finite cross section for charge exchange, some of these neutral atoms will lose their electrons to an energetic plasma ion. This newly-formed neutral atom will then continue with its same momentum, now unresponsive to the magnetic field lines that had confined it as an ion. It will quickly leave the plasma and penetrate into the first material

with which it has contact. At typical plasma ion energies (several keV), exposure to these sputtering neutrals will deteriorate an optical surface.

3.3 Two-Color Interferometer

The Two-Color Interferometer (TCI) on Alcator C-Mod was deployed in 1994 and initially used to measure transport coefficients [ref]. It has since become a "workhorse" diagnostic, responsible for the real-time density measurements that provide the feedback information for the gas fueling system. In addition, it is capable of generating density profiles that are often used in correlation with other density diagnostics. TCI operates as a heterodyne interferometer at 10.6 μm, with a second wavelength (633 nm) for vibration subtraction. The essential theory behind its operation is outlined in Chapter 2.

In practice, TCI generates a single elliptical beam by co-aligning the CO_2 and He-Ne beams and then expanding through a telescope of reflectors. This beam traverses the plasma vertically, entering through a gap in the lower divertor and exiting through a port on the top of the machine. A flat mirror reflects the beam back through the plasma with a slight toroidal offset that allows the return beam to be picked off, combined with the reference beam, and separated into wavelengths. The continuous elliptical beam is then segmented into discrete detector elements, ranging from 1 to 10 in CO_2 and 1 to 4 in Helium-Neon. The output from each of these detectors is mixed with a local oscillator and the phase is digitized by demodulators.

Figure 3.15 shows the portion of a typical C-Mod cross section included in the TCI view. While the system was designed to provide access from the plasma core to the outboard edge, incorrect collimation of the reference beam has reduced this range in

practice to the central channels. This limitation is caused by the size discrepancy between the plasma and reference beams (see inset of Figure 3.16), which are expanded independently.

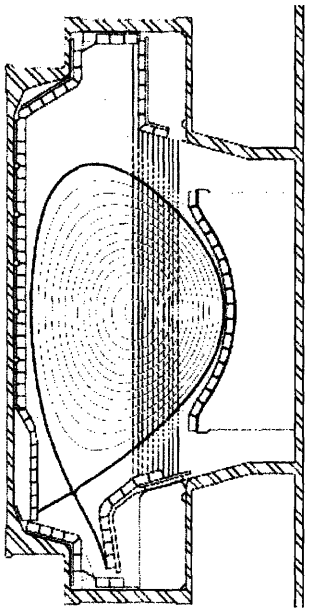

Figure 3.15 Representation of vertical TCI viewing chords through a C-Mod cross section

Figure 3.16 is a schematic of the polarimetry measurement made by modifying the TCI experiment. Because parts of the return beam were not utilized for density measurements, it was possible to pick off these portions and direct them through a simple polarimeter identical to that described in the PEM section above. The radiation source for TCI is a 60 W CO_2 laser produced by Coherent, with an output polarization horizontal to the plane of the optical table. The direction of the polarization acquires a small Faraday rotation (0.1-0.3°) over a double pass through the plasma, and this rotation is measured using the PEM technique.

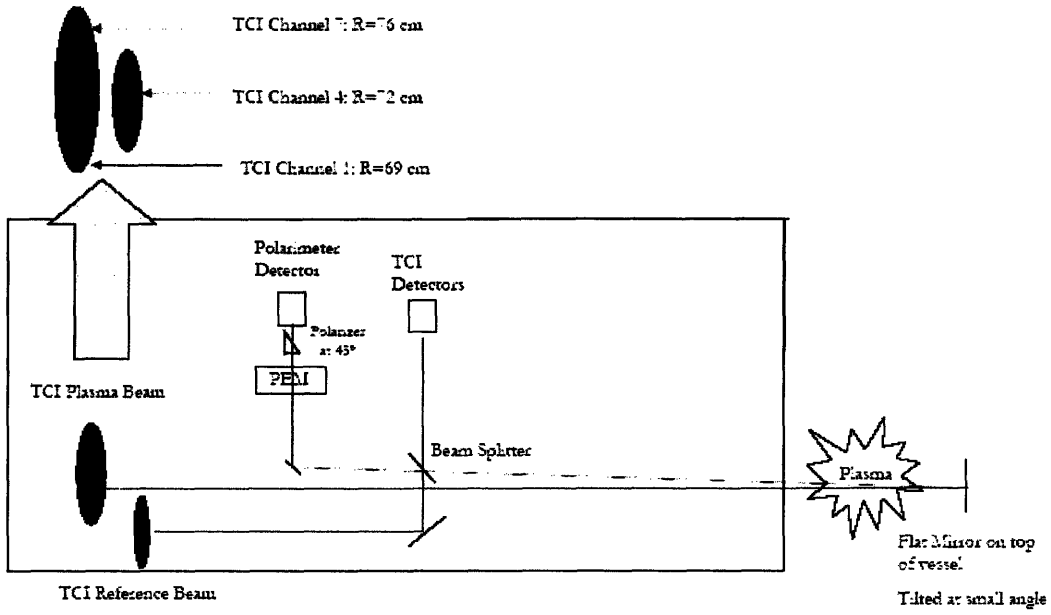

Figure 3.16 Optical layout of polarimetry measurement on TCI, with close up illustration of collimated plasma and reference beams

There are some subtleties in this measurement affecting the results presented in the next chapter. First, the presence of the reference beam in the detected optical chain was found to be deleterious to the measurement of Faraday rotation. Because the pickoff for this experiment occurs after the beam splitter where the plasma and reference beams are combined, fifty percent of the reference beam was also collected. Experimentally, the impact of this effect could be reduced by selectively blocking parts of the reference beam and aligning the detection system to view only the plasma beam. This method allowed accurate results to be obtained for the portion of the plasma beam corresponding to the outboard side of the plasma. However, data from the middle channels of the TCI view

were unavailable without incapacitating the interferometer for those channels. Because this would entail disabling the density feedback system, it was not done.

Second, the quality of the inboard part of the return beam, corresponding to the region near the plasma core, was prohibitively low. Although these channels were not in use and disabling the reference beam at this end of the beam was possible, there was not enough laser intensity to obtain reasonable signal. This, coupled with the miniscule parallel component of the magnetic field in this region, and the correspondingly small expected Faraday rotation signal, prevented good results from the region closest to the plasma core.

Chapter IV

Experimental Results

This chapter contains the results of the experiments described in Chapter 3. In presenting these results, the same sequence is followed. First, the interferometry measurements are discussed, followed by Faraday rotation results obtained using the counter-rotating beam configuration and the PEM configuration, respectively. Next, the condition of the retro-reflectors over the course of an Alcator C-Mod run campaign is discussed. Finally, the Faraday rotation data obtained with the vertical TCI view are presented and compared to a numerical model.

4.1 Interferometry

As described in Chapter 3, an interferometer was assembled with a poloidal view on Alcator C-Mod. This configuration was designed to test the feasibility of a future FIR polarimeter/interferometer that operates simultaneously, based on the three wavelength system discussed in the first chapter. In optical layout, it is almost identical to the existing interferometer (TCI), differing in viewing geometry and beam return mechanism. Successful measurements of line integrated density are described here. These measurements are of equal, and in some cases better, quality as those provided by the routine TCI diagnostic on C-Mod. In addition, the interferometer configuration provided valuable information about the experimental environment.

First, the interferometer configuration of the prototype polarimeter/interferometer provided reliable measurements of line-integrated density. Figure 4.1 displays a typical plasma discharge for Alcator C-Mod. The view for these data is a poloidal line of sight,

with reflection from Retro 4 as labeled in Chapter 3. The trace in the lower right is obtained through the poloidal interferometer. Note the qualitative similarities between this measurement and a trace obtained with the central TCI chord for the same time range, displayed in the upper left of the same figure. Because the TCI measurement is viewing closer to the center of the plasma and vertically traverses more plasma than the poloidal view, the corresponding line integrated values are 40-50% higher.

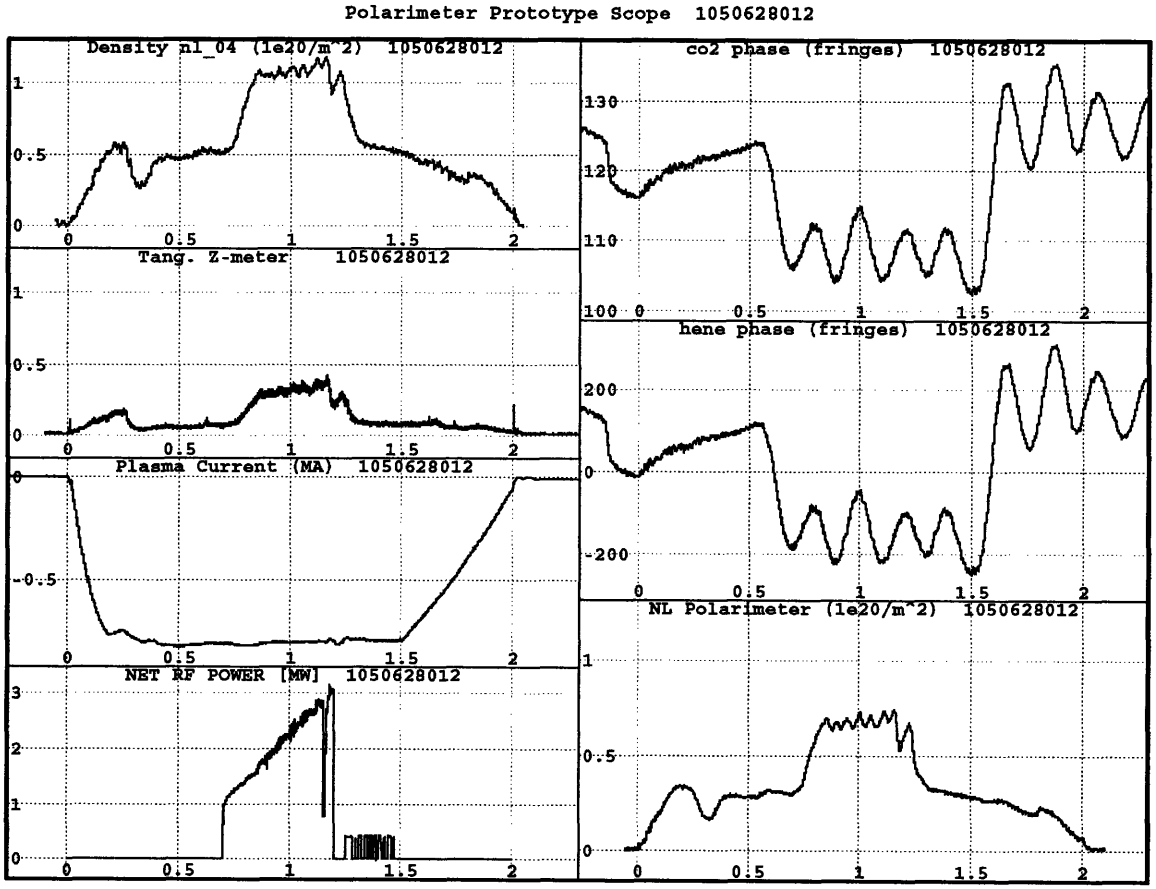

Figure 4.1 Interferometry measurement obtained with prototype system

In addition, the poloidal interferometer measured the movement of the inner wall during various experimental phenomena. Figure 4.2 displays diagnostic data representing

the final 10 milliseconds before a disruption, in which the plasma is quickly lost through a macroscopic instability. Shown on the left side are the sudden drop in density as measured by TCI (labeled "Density nl_04), a spike in effective charge number of the plasma (labeled Tang. Z-meter), the quick loss of toroidal plasma current, and the drop-off in injected RF power. The right column of Figure 4.2 contains interferometry data obtained by the poloidal polarimeter. Since the experimental layout involves reflection off the inner wall, the measured phase change includes a component due to the movement of the wall in the direction of beam propagation. In other words, the large vibrations of the tokamak inner wall change the path length of the system, and these changes can be quantified through interferometry.

Examination of the trace in the top right of Figure 4.2 reveals the phase shifts (almost all due to vibrational changes in path length) that occur during three phases of the discharge. Before the disruption (earlier than .915 s), the plasma is behaving normally with relatively steady current and density; the signal stays within a range of two CO_2 fringes, with noise less than one fringe. Each fringe corresponds to a change in path length equal to the laser wavelength, 10.6 μm. The second phase (0.915-0.920 s) involves the abrupt disruption of plasma current and density. This event causes a change in interferometry signal as large as 5 fringes in each direction, meaning that the path length (mostly due to movement of the inner wall) changes more than 0.1 mm. The third phase of the data (after 0.92 s) shows a recovery of signal over a few milliseconds, with the baseline returning to stability but with lingering noise of around two fringes (20 μm).

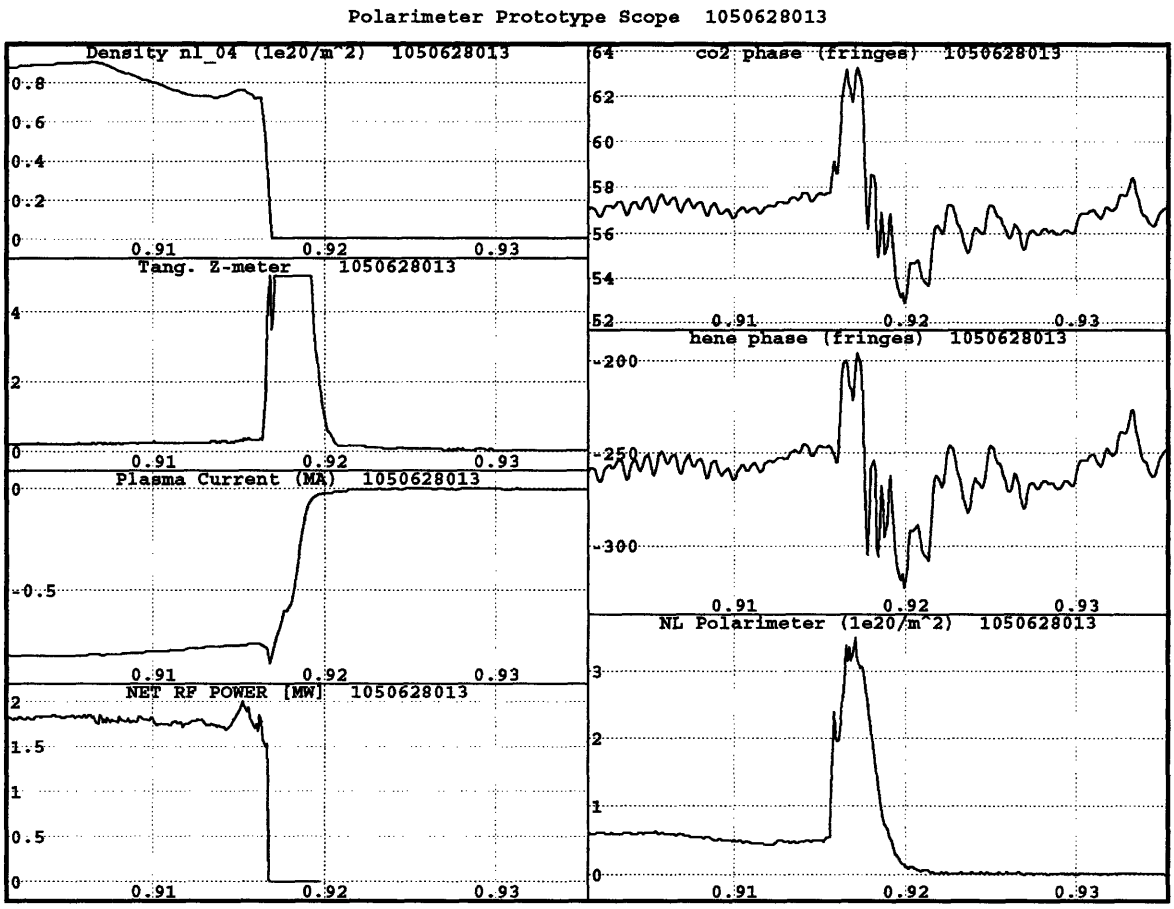

Figure 4.2 Measurement of inner wall movement during plasma disruption

Finally, the prototype polarimeter/interferometer was able to maintain signal during and after disruption events like the one described above. Because disruptions involve the discharge of large amounts of stored energy into the material surfaces surrounding the plasma, it can be expected that they cause significant experimental noise. They also correspond to rapid changes in plasma parameters that can be difficult for optical systems to track. Because of the rapid changes in density and the correspondingly large effects of refraction, disruptions often disable tracking by TCI, resulting in a loss of density feedback signal.

Figure 4.3 demonstrates interferometry data obtained over a longer time range during the same plasma discharge described above. The trace on the top left was obtained with TCI; note the loss of signal following the disruption (approximately 0.9 s). While the polarimeter phase signal shown in the top right spikes, it follows the disruption with steady (albeit noisy) tracking. This advantage could derive from geometry; the poloidal view is unaffected by the high volume of plasma particles that accumulate in the lower divertor as a result of disruptions.

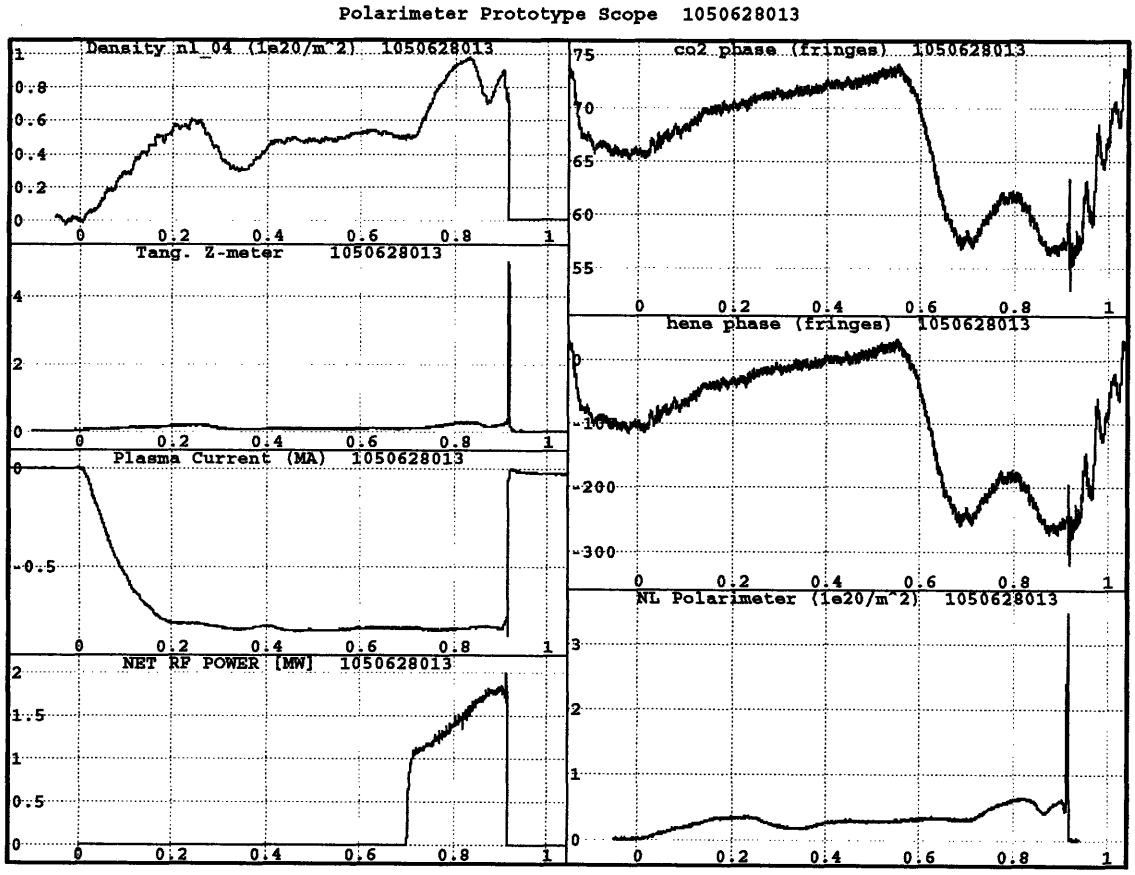

Figure 4.3 Interferometry measurements obtained with both TCI and prototype system during a disrupting plasma. Trace in top left is interferometry signal obtained with TCI, and trace in lower right is interferometry signal obtained with prototype.

4.2 Faraday rotation

As presented in Chapter 3, two methods for measuring Faraday rotation were examined. This section begins with a discussion of the counter-rotating beams configuration modeled after the Dodel-Kunz technique described above. This method was the first attempt chronologically, beginning operation toward the middle of the 2005 run campaign. Following a short period during which the interferometer configuration was employed, the prototype polarimeter was redesigned to employ the Kawano method based on Photoelastic Modulator (PEM) equipment. This section concludes with results obtained using the PEM configuration.

While the condition of in-vessel reflecting surfaces will be discussed later, it is important to mention here that reflectivity was limited by the gradual deterioration of these surfaces throughout the campaign. As a result, alignment became difficult and signals weaker. In addition, cracking of some of the optics restricted the available views through the plasma.

Figure 4.4 displays polarimetry data obtained using the counter-rotating beam configuration. These results were obtained using the reflector labeled "Retro 03" in Figure 3.12 and correspond to a view through the upper half of the plasma cross section. As shown on the left half of the figure, this plasma discharge has a line integrated electron density approaching $1x10^{20}$ m^{-3} and reaches a maximum current of almost 1 MA. The polarimetry measurement is found on the right side. The trace in the upper right shows the unprocessed Faraday rotation signal in degrees. Notice the variation of three to four degrees. In the middle display is the signal obtained by the reference detector described in Chapter 3. This detector monitors the variations in signal corresponding to

vibrations on the laser table itself. The trace on the lower right is the result of subtracting the reference signal from the original Faraday rotation signal. Although this subtraction and numerous additional attempts were made to understand and reduce this noise, it was never reduced below a degree with this experimental configuration. This signal has been summed over 50 ms windows to improve quality, but no significant advantage resulted from further averaging. Demands on experimental time resolution also impose a limit to realistic summing. In addition to the noise, the signal was observed to drift throughout the plasma discharge. These drifts surpassed the noise in magnitude, often reaching values of 2 degrees in rotation angle, and took place sporadically on a time scale of seconds and tenths of seconds.

A further purpose of the reference detector is to isolate the sources of noise and drifts. A trace of the polarization change (in degrees) recorded by this detector is found in the middle right portion of Figure 4.4. Through comparison of this signal with the normal Faraday rotation signal, it can be concluded that most of the noise and drifts are occurring on the optical table itself, as opposed to effects from the machine and plasma environment. This reference was examined in the context of the magnetic coils in the vicinity of the prototype experiment, suggesting a possible cause of the large noise observed. The lower two traces on the left side of Figure 4.4 show the current measurements from two neighboring coils. In addition, the RF input power and toroidal field magnitude are also displayed, as their respective infrastructures are positioned within range of potentially interfering with components of the prototype polarimeter and their signals sometimes correlated with drifts in rotation signal.

The reference signal was also used as an alignment tool and subtraction mechanism, making possible the best signal-to-noise ratios obtained with this technique. However, because of the size of the noise and drifts in comparison with the expected values of Faraday rotation, this method was ultimately unable to observe the effects of plasma in Alcator C-Mod.

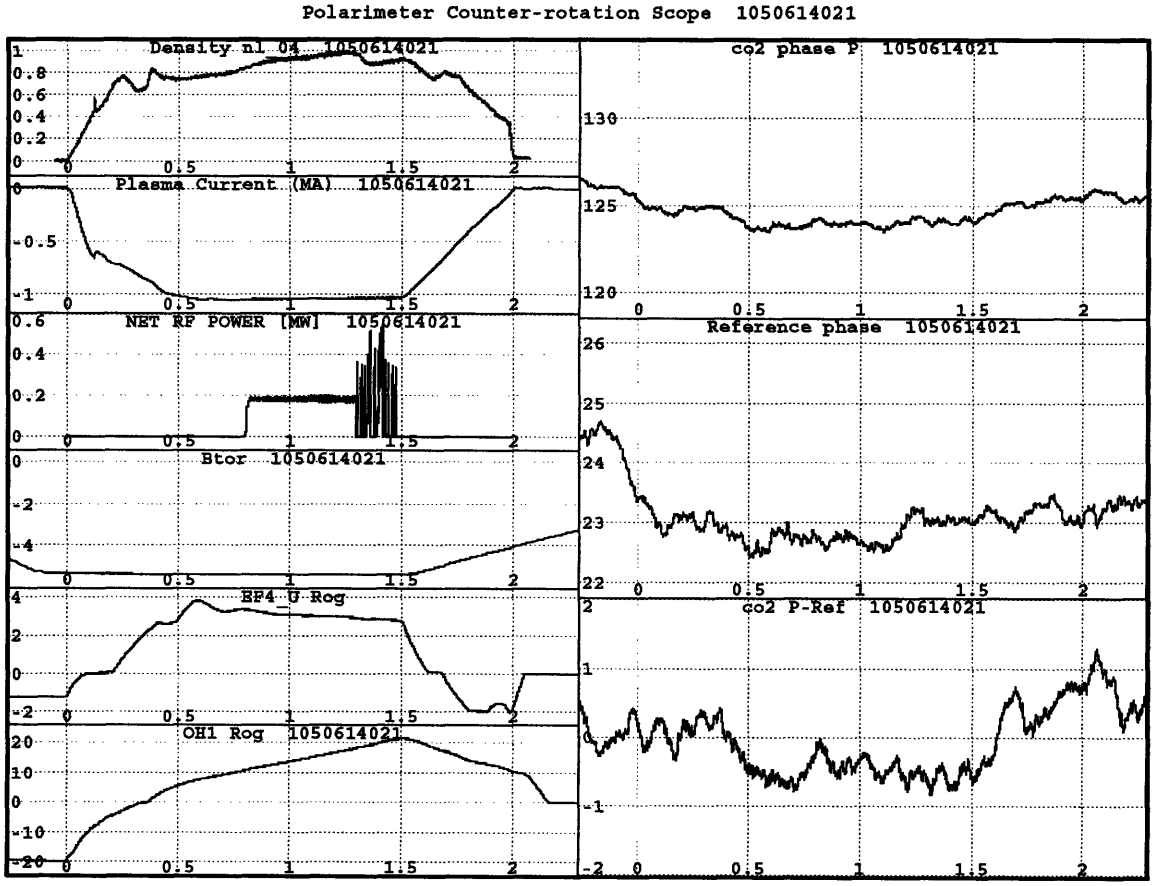

Figure 4.4 Faraday rotation measurements obtained with counter-rotating beam polarimeter configuration

The second configuration employed for measuring Faraday rotation is a straightforward polarimeter based on PEM technology for polarization analysis. It was found to be less sensitive to alignments, possibly because this design involves only one

laser beam to be injected into the plasma. Further, the PEM technique for measuring the return beam polarization allowed much smaller noise levels to be achieved, relative to the counter-rotating beam configuration discussed above. This technique was tested toward the end of the run campaign, when only one retro-reflector was available. The results below are consequently obtained using the reflector labeled Retro 06 in Figure 3.12. This imposes a viewing geometry that misses the plasma. However, the experimental conditions are expected to be comparable to the data obtained under the previous configuration, allowing a practical comparison between the two techniques.

Figure 4.5 displays diagnostic information from a plasma discharge similar to the one discussed above. While the maximum density, toroidal magnetic field, and injected RF power are the same as in the discharge displayed above, this plasma reaches only 750 MA of current. The traces in the right column correspond to polarimeter signals. The outputs of the lock-in amplifier (top two) measured the signal component at twice the modulation frequency, which are related to the Faraday rotation by Equation 2.34, repeated here for convenience:

$$\alpha = 93.8\frac{V_{2f}}{V_{DC}}$$

The third trace is the signal from the detector with no analysis. This is the DC signal used for normalization in the expression above. The signal displayed in the lower right is the calculated Faraday rotation angle. Notice that the noise in this signal is much smaller than that measured with the counter-rotating technique, around 0.1°, with a drift of as much as 0.5° during the course of the plasma discharge. These results were obtained using data averaging to the same 50 ms time resolution as employed above. Approximately half of the experimental noise under this configuration was determined to

be originated on the optical table itself, with the values presented here demonstrating the best performance obtained.

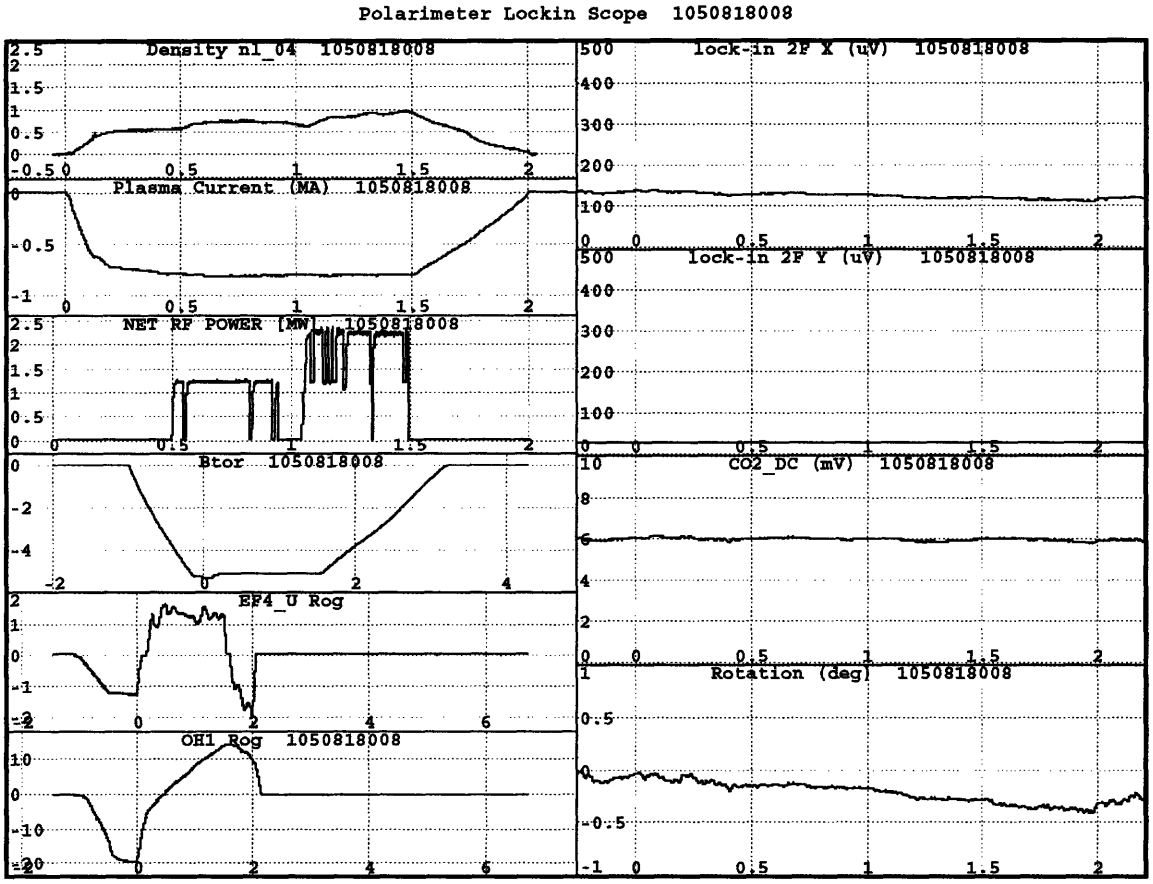

Figure 4.5 Faraday rotation measurements obtained using the PEM polarimeter configuration. Trace in lower right is Faraday rotation in degrees.

The two methods for measuring Faraday rotation described here involve different experimental apparatus and alignment techniques, and yield different results. The two relevant traces for comparison are found in the lower right of Figures 4.4 and 4.5, where measured Faraday rotation is expressed in degrees in both cases. For the prototype polarimeter discussed in this thesis, the PEM method was found to perform better; the advantages in signal-to-noise and drifts were roughly an order of magnitude. This result

is consistent with the choice of the Kawano group to use PEM analysis for their CO_2 laser polarimeter.

The counter-rotating beam technique was found to be experimentally challenging. One potential reason for this difficulty is the extreme sensitivity inherent in this design to the co-alignment of the two counter-rotating laser beams over a long path. While the number of surfaces unique to each of these beams was minimized, there is an inevitable difference in path required to generate the necessary polarizations. This difference introduces a minimum noise level that is not existent in the PEM configuration.

4.3 Retro-reflectors

As discussed in Chapter 3, the survival and functionality of the in-vessel retro-reflectors over time is one of the primary goals of this work. By observing the six reflectors remotely throughout the run campaign, and then thoroughly examining them after the campaign, analysis of their condition was possible. The results below are organized by phenomenon and presented in the same order as in Chapter 3.

First, thermal conditions affected the retro-reflectors. Thermally-induced expansion and contraction of the various constituent materials with respect to each other resulted in movements of optical surfaces sufficient to destroy alignment. Alignment loss due to thermal effects was characterized by changes over several hours, repeated in trends from day to day. Typically, alignment of the system was touched up in the morning, when the inner wall temperature was at its highest (before the cooling of the magnetic coils). As the inner wall was liquid-nitrogen cooled throughout the day, signal levels gradually worsened until it became necessary to enter the tokamak cell and optimize alignment.

In addition to deterioration in optical alignment, thermal gradients also resulted in permanent damage to two of the retro-reflectors. In each of these instances, the retro-reflector lost functionality in a sudden event. The break was discovered by a missing return beam from one of the reflectors, confirmed by sight through the vacuum vessel window, and then examined in greater detail after the opening of the vessel. Figure 4.6 is a photograph of Retro 05, which cracked just a few weeks before the end of the run campaign. Notice the missing segment of the three-part assembly and the cracked remnants lying in the bottom of the cylindrical container.

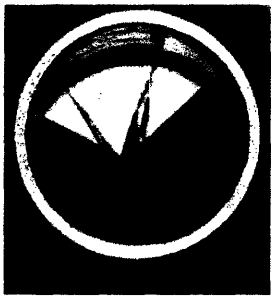

Figure 4.6 Photograph of a retro-reflector that cracked because of thermal forces

Another effect observed to deteriorate reflective surfaces is coating by dust and boron. As explained in Chapter 3, the ambient dust in typical plasmas and the diborane applied to the material surfaces of the vessel for increased experimental performance are both deposited on the optical surfaces. This coating destroys reflectivity, analogous to a mirror accumulating dust on a shelf. All six retro-reflectors were coated with dust and boron when examined after the run campaign, with the most damage occurring to those positioned closest to the plasma midplane. Unique to the run campaign during which these retro-reflectors were employed was the installation and subsequent decomposition of a titanium-coated coupler, part of the Lower Hybrid Current Drive program on C-Mod.

Several kilograms of titanium dust were discovered in the vacuum vessel, and this could explain the large amount of dust particles found on the reflecting surfaces. Figure 4.7 is a photograph of Retro 04 taken after the run campaign. The coatings on the surfaces are especially evident when compared to a new reflector (see Figure 3.13). A magnified image of another retro-reflector is found in Figure 4.8. With this resolution, it is possible to see individual dust particles on the mirror surface.

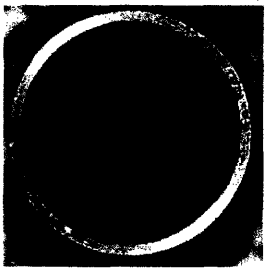

Figure 4.7 Photograph of a retro-reflector coated by dust and boron

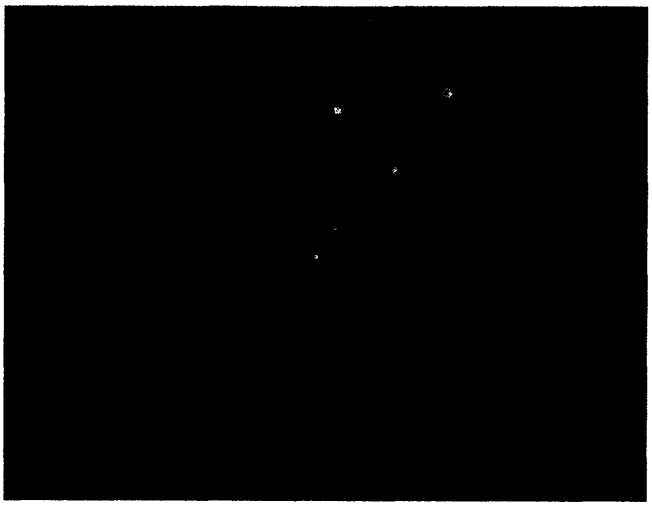

Figure 4.8 Close-up of dust accumulation on retro-reflector surfaces

The third phenomenon that affected the in-vessel optical surfaces is plasma sputtering. Since this effect involves the ejection of energetic neutral particles from the

plasma itself, it is reasonable to expect its influence to be most pronounced on the surfaces closest to the plasma. This expectation was verified experimentally; the degree of damage discovered varied with location in the vessel and was most severe in the two retro-reflectors closest to the plasma midplane. Further, the areas damaged by sputtering are the outer edges of the reflecting surfaces, which did not have the protection of the containing cylinder or the neighboring tiles. Figure 4.9 is a photograph of Retro 01, positioned only a few centimeters from the toroidal axis of the tokamak. The damage caused by neutral sputtering is apparent in the close-up image found in Figure 4.10, taken from the same reflector. Here the same curved boundaries are evident, with other regions of destroyed surface closer to the center, caused by the most energetic neutrals leaving the plasma.

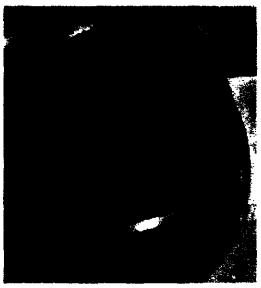

Figure 4.9 Photograph of retro-reflector damaged by plasma sputtering

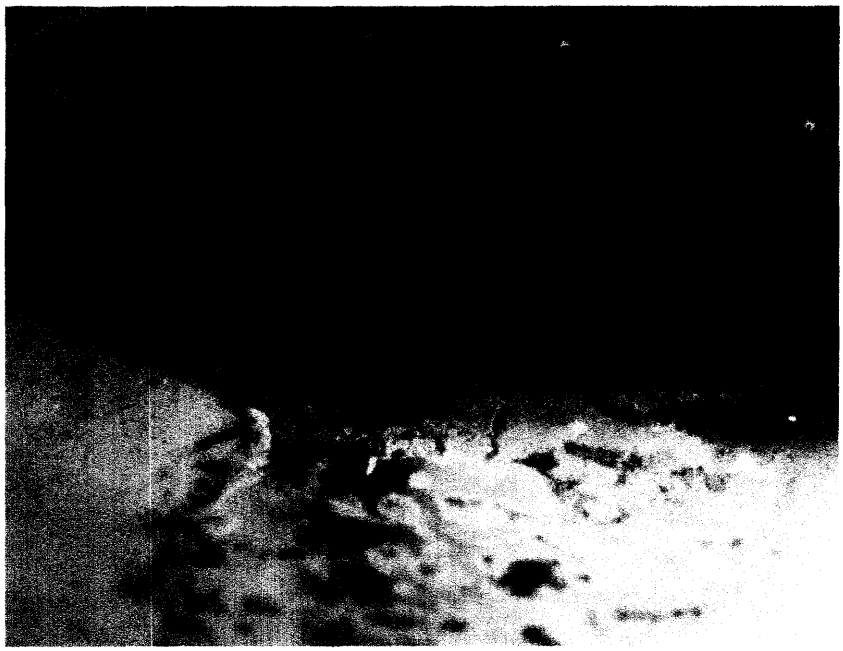

Figure 4.10 Close-up of effects of plasma neutrals on retro-reflector surface

4.4 TCI Measurements

In addition to the interferometry and polarimetry results presented above, a separate measurement was made possible by a modification to the TCI experiment on Alcator C-Mod. Because TCI has a vertical plasma view, there are no in-vessel optics employed in these results. Further, the optical table, components and beam path are part of a regularly used diagnostic system, providing an experimental environment with sufficiently low noise as to enable Faraday rotation measurements to be made at 10.6 μm.

Typical rotation angles reached 0.2-0.3°, and time evolution of this signal followed the plasma density. An example of a plasma discharge is displayed in Figure 4.11. In this case, current slowly ramps to a flat plateau at roughly 800 kA, then ramps down over the last half second of the discharge. A spike in several of the signals displayed corresponds to the injection of a pellet into the plasma between 1.6 and 1.7 s. The pellet causes a sudden rise in density, apparent in the line integrated TCI signal (top

right) and the Faraday rotation signal (second to top on right). As derived in Chapter 2, Faraday rotation depends on the product of parallel field and electron density along the path of the laser. The signals displayed here also indicate periods of high confinement known as H-modes, evidenced by rises in the plasma density and by perturbations in the spectroscopy signals monitoring lines from Hydrogen (second from top on left) and ionized Carbon (third from top on left). These periods take place when RF power is being injected into the plasma; in this case, 3 MW were injected from approximately 0.7 to 1.4 seconds (lower left).

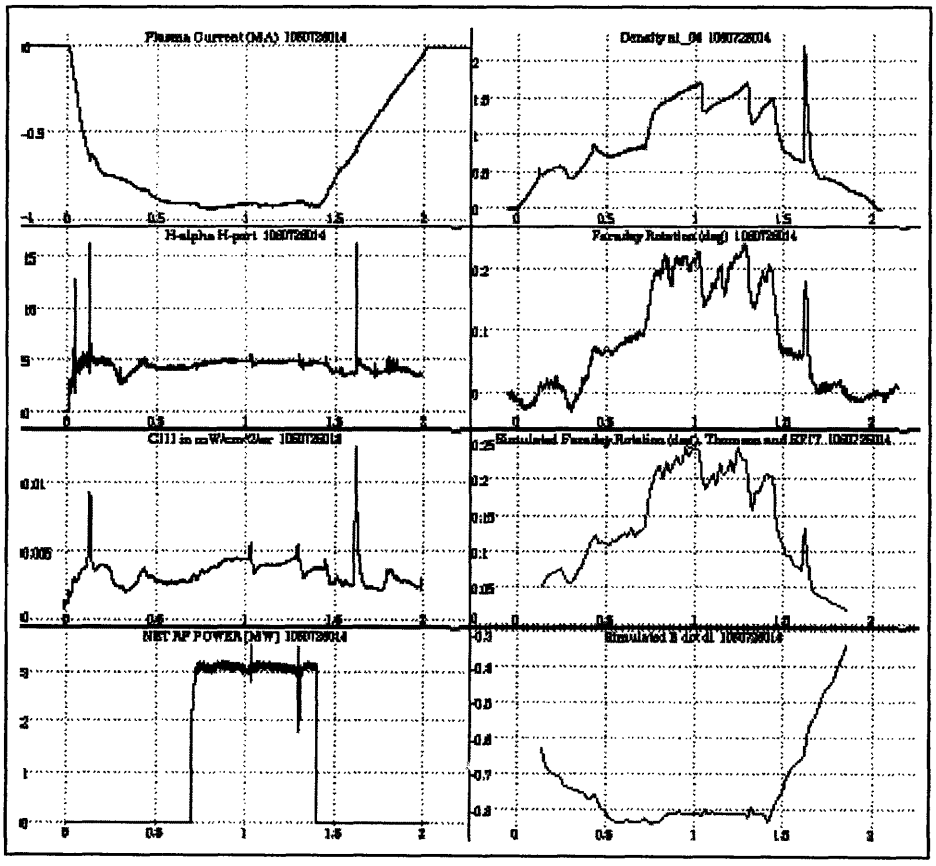

Figure 4.11 Faraday rotation measurement performed using TCI infrastructure and view

The lower two traces on the right are calculated values for expected Faraday rotation and line integrated magnetic field component along the direction of beam propagation, respectively. To produce these expected signals, a numerical model was created using EFIT reconstructions, Thomson scattering density profiles, and a measured value of chord location in the direction of major radius. Each of these inputs to the model will be discussed briefly here.

As described in Chapter 1, EFIT is the two-dimensional equilibrium fitting routine operational on Alcator C-Mod. This code applies the measurements made by magnetic coils near the plasma edge as imposed boundary conditions, and then iteratively solves the Grad-Shafranov equation governing plasma MHD equilibrium. As noted above, EFIT requires assumptions to be made about the poloidal magnetic field in order to generate its profiles. For the reconstructed field profiles employed in this model, a shaped current profile was assumed. This assumption is generally acceptable for slow-changing plasmas, but breaks down for rapid events as well as external current drive (Lower Hybrid system on Alcator C-Mod).

In addition to the magnetic field profile, a density profile is required to obtain a model of Faraday rotation. The profiles used here are fits to the Thomson scattering data routinely generated on Alcator C-Mod. Because the Thomson scattering profiles are based on local measurements, the ambiguity associated with the inversion of interferometry data was avoided.

Finally, the position of the laser view relative to the plasma is necessary to allow comparison between the numerical model and the empirical results. Although correlation with the TCI system was accessible by viewing the location of the picked off beam used

for polarimetry on the detector array, the absolute positions of the TCI chords was uncertain to within a few centimeters. To confirm the beam location, a mask on the visible laser beam could be viewed on the final mirror before entrance into the vacuum vessel. This mirror has been used in the past for TCI calibration, and its position is accurately known to within a millimeter. Because the optical aperture entering the polarimeter system is on the order of 5 mm, the measurement of the beam position on this calibrated mirror was accurate to one centimeter.

These inputs are combined in a straightforward manner to calculate the Faraday rotation expected for a given plasma. The approach is based on the expression for Faraday rotation (Eq. 2.24) derived above, taking into account the density and field component parallel to the direction of beam propagation, and integrated along a specified path. This path is chosen in the two-dimensional plane based on the measured chord location. The EFIT reconstruction provides the field magnitude and direction for each location along the laser path; the parallel component is easily calculated. In order to obtain plasma density at each point along the path, a flux surface model is applied, in which the density is assumed to be constant on each nested flux surface. On the timescales for which MHD equilibrium is a valid assumption, this model is reasonable because of the fast diffusion of particles along magnetic field lines. The Faraday rotation is calculated by multiplying the parallel field component, density, and a scaling factor and summing for small steps in the vertical direction.

Because of the uncertainty introduced through the three inputs described above, the model employed here is not expected to exactly agree with measurements. In addition, the polarimeter signal itself has a noise level of several hundredths of a degree

at the time resolution desired. Nevertheless, a qualitative agreement between the model and experiment was observed, as displayed in Figure 4.12. Here the pink line represents the calculated Faraday rotation, and the black trace is obtained empirically.

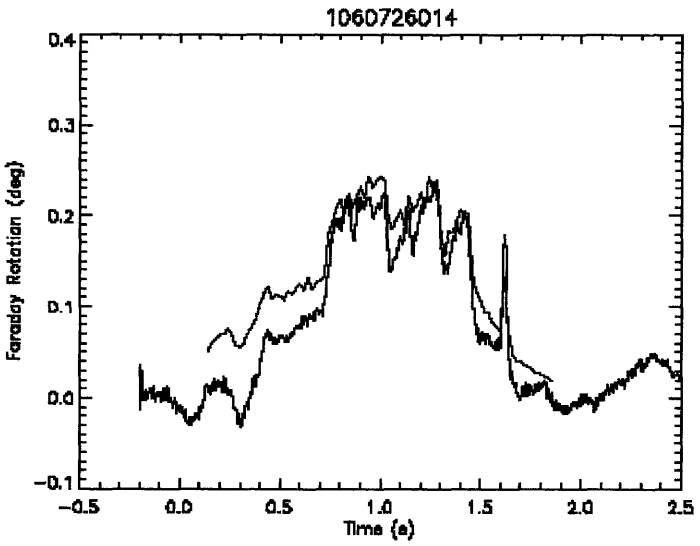

Figure 4.12 Comparison between model (pink) and experiment (black) for Faraday rotation with vertical (TCI) view

Chapter V

Conclusion

This chapter summarizes the experimental results presented above, emphasizing those most applicable to future work. As stated in the introduction, the purpose of the prototype polarimeter/interferometer reported in this thesis is to assess experimental factors that will affect the FIR polarimeter/interferometer, planned to be installed for FY2008 on Alcator C-Mod. In addition to the summary and application of results, this chapter concludes with a discussion of improvements to the prototype system for further investigation. To conclude, the discussion of the future FIR system introduced in Chapter 1 is extended in the context of this work and its applications.

5.1 Application of results to FIR polarimeter

Because of the small expected signal in Faraday rotation for the geometry and wavelength employed, as well as the experimental difficulties associated with a new optical system and in-vessel retro-reflectors, it was not surprising that no Faraday rotation could be made by the prototype. Noise levels lower than 0.1° were never achieved, and drifts in signal were roughly five times larger. Both of these problems made the measurement of an expected 0.1° rotation impossible. Because the signal size varies with the square of wavelength, the factor of ten increase to the FIR wavelength (119μm) will mean a factor of 100 in Faraday rotation. Tens of degrees will be much easier to measure.

However, comparison between the two measurement techniques was possible, resulting in useful information about experimental methods. The PEM technique was

consistently better in terms of noise and drift than the counter-rotating beam technique. This advantage held up even after significant efforts to improve the stability of alignment of the two beams in the latter configuration. Essentially, the quality of results was found to be very sensitive to the relative alignment of the two laser beams with opposing circular polarizations. Since the FIR system will involve a similar scheme to the counter-rotating beam method tested in this work, it is crucial that alignment be analyzed and optimized in order to produce a reliable diagnostic system. Specifically, the optical path lengths traveled by the two beams independently must be minimized and, if possible, mechanically coupled to reduce the deleterious effects of vibrational misalignment. In addition, the optical system should be designed to allow for the viewing of the two co-aligned beams over long distances. This alignment should take place before the beginning of a run campaign, but should also be repeated throughout the following weeks of operation, and even throughout a run day. Because of the protocols restricting access to the Alcator C-Mod cell, this alignment will need to be performed remotely.

The interferometry results reported in the last chapter provide useful information for the design of the FIR polarimeter/interferometer system. First, this measurement quantifies the change in optical path associated with experimental noise during a plasma discharge. Because the inner wall movement can account for as many as 10 CO_2 fringes, it can be concluded that some form of vibrational correction be employed for the FIR system, which has a wavelength roughly ten times larger than the CO_2 prototype. A mechanism for vibration subtraction similar to that used on TCI seems intuitive; however, the wide differences in available optics for the two wavelengths make this a non-trivial question.

In addition to measuring the movement of the inner wall, the prototype interferometer tested the experimental durability of an optical system reflecting from the tokamak inner wall. The interferometer proved to be more stable against large plasma events like disruptions, suggesting that avoiding the divertor region is advantageous for polarimetry and interferometry.

The condition of the retro-reflectors after a complete run campaign was also an important test. As explained above, the inner wall of a tokamak is a harsh environment for optical surfaces. Nevertheless, in order to obtain a poloidal view and avoid the diverter region, while conserving port space, the designs for future FIR polarimeter/interferometers rely on the successful, long-term performance of these optics. While the retro-reflectors certainly experienced damage over the course of the campaign, they performed up to, or perhaps exceeded the expectations for a commercially purchased product lying virtually unprotected on the inner wall. Several improvements to the retro-reflector assembly (explained below) are expected to show the survivability of inner wall optics through periods of many months and hundreds of seconds of plasma.

Finally, the Faraday rotation results obtained on the TCI experiment match the numerical model reasonably well, suggesting that Faraday rotation was indeed observed on Alcator C-Mod, albeit under a different geometry than that primarily intended. From this experiment, two conclusions can be drawn. First, Faraday rotation can be observed to fall within expected values of a few tenths of a degree. Second, the PEM technique for measuring the change in polarization can reach accuracies close to those reported in the literature, with noise levels of a few hundredths of a degree. With further work, Faraday rotation could feasibly be observed by the prototype with the poloidal geometry, although

not as a reliable measurement. The next section discusses the future work to take place on the prototype polarimeter before the installation of the FIR system in 2008.

5.2 Future work on prototype system

As reported above, much of the experimental noise and signal drifts was a result of mechanical vibrations in the optical table itself. In addition, mode instability in the source CO_2 laser was a limiting factor. As evidenced by the results obtained on TCI, both noise and drift levels can be drastically reduced by improving the mechanical stability of the table and the mode stability of the laser. To these ends, a new optical table and a scientific-grade CO_2 laser were obtained for the prototype polarimeter, both to begin use in the FY2007 run campaign. In addition, new solid-state, thermo-electric detectors have been installed. These detectors are capable of measuring laser intensities as low as a few milliwatts, while the previous detectors could not resolve signals below a few hundred mW. Performance of the laser table portion of the polarimeter system is expected to increase significantly as a result of these equipment upgrades.

The in-vessel optics are also a crucial part of the optical system. To protect them and extend their lifetime, several improvements are underway. First, efforts have been initiated to construct the retro-reflectors out of the same material. While difficult from an engineering perspective, all-metal optics would expand and contract as a solid body, preventing the breaking of parts and consequent contamination of the vacuum vessel with shards of glass and other materials. Second, a shutter assembly has been designed and installed to protect the optics during the coating of the vessel walls with diborane, or during situations where plasma events along the inner wall are expected. The shutter is driven by a hydraulic mechanism which can be remotely controlled and is expected to

function through hundreds of cycles. Finally, the reflecting surfaces have been withdrawn three millimeters from their original location, restricting solid angle for potentially damaging energetic particles.

The prototype polarimeter will be further modified to include a new active alignment system based on piezoelectric positioners. This active alignment technique will be tested for use on the FIR polarimeter/interferometer. As discussed above, both thermal and environmental conditions lead to slow changes in alignment throughout a day. In addition, faster misalignments lead to signal drifts on the order of a few Hertz. To correct for these alignment problems, a position-sensitive detector will be installed to monitor the position of the return beam after it traverses the plasma. The signal from this detector will be fed to a Piezoelectric Transducer (PZT) in the optical path, which will make small corrections in alignment at timescales as fast as a few tens of Hertz. This system should reduce the observed drifts in the signals displayed above. It is also expected to eliminate the need for cell access in between plasma discharges and thereby make the FIR polarimeter more robust as a diagnostic tool.

5.3 FIR system

The work reported in this thesis was performed in preparation for a Far-infrared (FIR) polarimeter/interferometer on Alcator C-Mod. This experiment will provide information about the poloidal magnetic field that can be combined with the EFIT reconstruction tool, resulting in accurate, two-dimensional current profiles. As discussed in the first chapter, an understanding of the current profile will contribute to the study of many plasma effects. This section describes the current plan for the FIR system.

Figure 1.5 is a diagram of the proposed laser chords for the FIR polarimeter/interferometer. With twenty chords spanning the poloidal cross section of the plasma, magnetic field information will be deduced through inversion to the required spatial resolution. These distinct chords are expected to be produced by a series of small reflectors in the path of a single, expanded beam. By independent control of each of these mirrors, each beam can be directed along a unique path and returned via a retro-reflector on the inner wall.

The light source for this experiment is expected to be a three-wavelength FIR laser with a central wavelength of 119 μm, and two other beams with offsets on the order of hundreds of nanometers. Two of the beams will be given opposing circular polarizations and combined to probe the plasma and return a value of Faraday rotation, as in the counter-rotating design discussed above. The third wavelength allows interferometry to be simultaneously performed. After inversions, correlation with other diagnostics and iteration with the EFIT routine, this system will produce poloidal profiles of both density and current.

While the primary advantage of increased signal size justifies the wavelength choice of 119 μm, there are several experimental factors to consider in applying the results of the prototype experiment described here to future work. First, refraction becomes more significant at larger wavelength, resulting in greater alignment difficulty, as well as uncertainty about the absolute position of the measurement's line of sight. While values of refraction for typical C-Mod parameters result in less than 0.1 mm of beam displacement at 10.6 μm, the same calculation performed for 119 μm predicts displacements as large as a millimeter. Although this is probably acceptable for the

resolution desired, it shows the importance of monitoring refraction in the experimental environment and considering the changes in refraction that will result from non-standard plasmas (high density, etc).

Another factor to consider is the Cotton-Mouton effect. Essentially, this effect results in an ellipticity introduced to the polarization of the probing laser beam when it propagates perpendicular to the magnetic field, rather than parallel. In the theoretical discussion in Chapter 2, it was determined that the characteristic polarizations are circular when the quantity $\frac{\omega_{ce}}{\omega}\sec\theta$ is small. At 10.6 μm, the ratio of frequencies (assuming a magnetic field of 5 Tesla) is 0.005. For this wavelength, the model described above is valid for all angles except those very near perpendicular. For example, if the angle between laser propagation and the magnetic field is 88°, then the quantity of interest is 0.14.

However, the same quantity for 119 μm is 0.056, and angles as far from perpendicular as ten degrees give values comparable to unity. For these cases, a more sophisticated treatment must be applied. While not carried out here, the details are available in the Hutchinson textbook referenced above [22]. The result of this more complete derivation of Faraday rotation is a new parameter representing the angle between the polarization of the input beam and the magnetic field. If this angle is sufficiently small, the model described above continues to be valid. In other words, the ellipticity applied to the polarization (the Cotton-Mouton effect) can be neglected. For an anticipated FIR polarization in the same direction as that of the prototype system, the new factor to consider is roughly 0.17. This, multiplied by the quantity $\frac{\omega_{ce}}{\omega}\sec\theta$ must now

remain much smaller than one for the model to be valid. As a result, the normal treatment of Faraday rotation will be adequate for typical plasma parameters and for most viewing chords. Only those chords that pass closest to the plasma midplane (and hence perpendicular to the magnetic field lines) will be significantly affected. However, the Cotton-Mouton effect requires that significant care be taken to understand the theoretical subtleties behind the measurement and consequent results.

References

[1] European Fusion Development Agreement Website, www.efda.org

[2] G. Gammel et. al., Rev. Scientific Instruments **57** (8), 1800, (1986).

[3] F. M. Levinton et. al., Phys. Rev. Lett. **63** 2060, (1989).

[4] L. L. Lao, Nucl. Fusion **30** (6), 1035, (1990).

[5] F. De Marco and S. E. Segre, Plasma Phys., **14** (3), (1972).

[6] W. Kunz, Nucl. Fusion **18**, 1729, (1978).

[7] A. R. Jacobson, Los Alamos National Lab Report No. LA-6875-MS, (1977).

[8] D. Veron, in *Infrared and Submillimeter Waves*, K.J. Button ed., Vol. 2. New York: Academic Press, (1979).

[9] H. Soltwisch, Nucl. Fusion **23** (12), 1681 (1983).

[10] G. Braithwaite et al., Rev. Scientific Instruments **60** (9), 2825 (1989).

[11] H. Soltwisch, Rev. Scientific Instruments **57**(8), 1939, (1986).

[12] J. O'Rourke, Plasma Phys. Controlled Fusion **33** (4), 289 (1991).

[13] H. Soltwisch, Proceedings of International School of Plasma Physics, Piero Caldirola, Varenna, 75, (1991).

[14] D. Brower et al., Rev. Scientific Instruments **72** (1), 1077 (2001).

[15] D. Brower et al., Phys. Rev. Lett. **88**, 185005 (2002).

[16] F. C. Jobes and D. K. Mansfield, Rev. Scientific Instruments **66** (1), 386 (1995).

[17] Kawano et al., Rev. Scientific Instruments **72** (1), 1068 (2001).

[18] Alcator Staff, Alcator C-Mod Fusion Research Program 2003-2008, Volume I, Technical Proposal, (2003).

[19] Alcator Group, The physics and engineering of Alcator C-Mod, Technical Report. PFC/RR-88-11, MIT Plasma Science and Fusion Center, (1988).

[20] P. Bonoli et al., Nucl. Fusion **40** (6), 1253, (2000).